J. Fluid Mech. (2010), *vol.* 650, *pp.* 181–214. © Cambridge University Press 2010
doi:10.1017/S0022112009993703

Global three-dimensional optimal disturbances in the Blasius boundary-layer flow using time-steppers

ANTONIOS MONOKROUSOS, ESPEN ÅKERVIK, LUCA BRANDT† AND DAN S. HENNINGSON

Linné Flow Centre, KTH Mechanics, SE-100 44 Stockholm, Sweden

(Received 12 May 2009; revised 27 November 2009; accepted 27 November 2009; first published online 18 March 2010)

The global linear stability of the flat-plate boundary-layer flow to three-dimensional disturbances is studied by means of an optimization technique. We consider both the optimal initial condition leading to the largest growth at finite times and the optimal time-periodic forcing leading to the largest asymptotic response. Both optimization problems are solved using a Lagrange multiplier technique, where the objective function is the kinetic energy of the flow perturbations and the constraints involve the linearized Navier–Stokes equations. The approach proposed here is particularly suited to examine convectively unstable flows, where single global eigenmodes of the system do not capture the downstream growth of the disturbances. In addition, the use of matrix-free methods enables us to extend the present framework to any geometrical configuration. The optimal initial condition for spanwise wavelengths of the order of the boundary-layer thickness are finite-length streamwise vortices exploiting the lift-up mechanism to create streaks. For long spanwise wavelengths, it is the Orr mechanism combined with the amplification of oblique wave packets that is responsible for the disturbance growth. This mechanism is dominant for the long computational domain and thus for the relatively high Reynolds number considered here. Three-dimensional localized optimal initial conditions are also computed and the corresponding wave packets examined. For short optimization times, the optimal disturbances consist of streaky structures propagating and elongating in the downstream direction without significant spreading in the lateral direction. For long optimization times, we find the optimal disturbances with the largest energy amplification. These are wave packets of Tollmien–Schlichting waves with low streamwise propagation speed and faster spreading in the spanwise direction. The pseudo-spectrum of the system for real frequencies is also computed with matrix-free methods. The spatial structure of the optimal forcing is similar to that of the optimal initial condition, and the largest response to forcing is also associated with the Orr/oblique wave mechanism, however less so than in the case of the optimal initial condition. The lift-up mechanism is most efficient at zero frequency and degrades slowly for increasing frequencies. The response to localized upstream forcing is also discussed.

† Email address for correspondence: luca@mech.kth.se

https://doi.org/10.1017/S0022112009993703 Published online by Cambridge University Press

1. Introduction

The flat-plate boundary layer is a classic example of convectively unstable flows; these behave as broadband amplifiers of incoming disturbances. As a consequence, a global stability analysis based on the asymptotic behaviour of single eigenmodes of the system will not capture the relevant dynamics. From this global perspective, all the eigenmodes are damped, and one has to resort to an input/output formulation in order to obtain the initial conditions yielding the largest possible disturbance growth at any given time and the optimal harmonic forcing. To do this, an optimization procedure is adopted. The aim of this work is to investigate the global stability of the flow over a flat plate subject to external perturbations and forcing and to examine the relative importance of the different instability mechanisms at work. The approach adopted here can be extended to any complex flow provided a numerical solver for the direct and adjoint linearized Navier–Stokes equations is available.

Recently, the global stability of the spatially evolving Blasius flow subject to two-dimensional disturbances has been studied within an optimization framework by projecting the system onto a low-dimensional subspace consisting of damped Tollmien–Schlichting (TS) eigenmodes (Ehrenstein & Gallaire 2005). These results were extended by Åkervik *et al.* (2008), who found that by not restricting the spanned space to include only TS modes, the optimally growing structures could exploit both the Orr and the TS wave packet mechanism and yield a substantially higher energy growth. The Orr mechanism (Orr 1907) was studied in the context of parallel shear flows using the Orr–Sommerfeld/Squire (OSS) equations by Butler & Farrell (1992), who termed it the Reynolds stress mechanism. This instability extracts energy from the mean shear by transporting momentum down the mean momentum gradient through the action of the perturbation Reynolds stress. In other words, disturbances that are tilted against the shear can borrow momentum from the mean flow while rotating with the shear until they are aligned with it. This mechanism is also referred to as wall-normal non-normality.

From the local point of view, the TS waves appear as unstable eigenvalues of the Orr–Sommerfeld equation. In the global framework, however, the global eigenmodes belonging to the TS branch are damped (Ehrenstein & Gallaire 2005), and the evolution of TS waves consists of cooperating global modes that produce wave packets. Considering the model problem provided by the Ginzburg–Landau equation with spatially varying coefficients, Cossu & Chomaz (1997) demonstrated that the non-normality of the streamwise eigenmodes resulting from the local convective instabilities leads to substantial transient growth. This non-normality is revealed by the streamwise separation of the direct and adjoint global modes induced by the basic flow advection; it is therefore also termed streamwise non-normality (Chomaz 2005).

It is now well established that when incoming disturbances exceed a certain amplitude threshold, the flat-plate boundary layer is likely to undergo transition due to three-dimensional instabilities arising via the lift-up effect (Ellingsen & Palm 1975; Landahl 1980). This transient growth scenario, where streamwise vortices induce streamwise streaks by the transport of the streamwise momentum of the mean flow, was studied for a variety of shear flows in the locally parallel assumption (cf. Butler & Farrell 1992; Reddy & Henningson 1993; Trefethen *et al.* 1993). The extension to the non-parallel flat-plate boundary layer was performed at the same time by Andersson, Berggren & Henningson (1999) and Luchini (2000) by considering the steady linear boundary-layer equations parabolic in the streamwise direction. In these investigations, the optimal upstream disturbances are located at the plate leading edge

https://doi.org/10.1017/S0022112009993703 Published online by Cambridge University Press

and a Reynolds-number-independent growth was found for the evolution of streaks at large downstream distances. Levin & Henningson (2003) examined variations of the position at which disturbances are introduced and found the optimal location to be downstream of the leading edge. In this study, low-frequency perturbations were also considered, which are still within the boundary-layer approximation. In the global framework, an interpretation of the lift-up mechanism is presented e.g. by Marquet *et al.* (2008): Whereas the TS mechanism is governed by a transport of the disturbances by the base flow, the lift-up mechanism is governed by a transport of the base flow by the disturbances. Inherent in the lift-up mechanism is the component-wise transfer of momentum from the two cross-stream to the streamwise velocity component (component-wise non-normality).

The standard way of solving the optimization problems involved in the determination of optimal initial condition (or forcing) is to directly calculate the matrix norm of the discretized evolution operator (or the pseudo-spectrum of the resolvent) of the system. In the local approach, in which the evolution is governed by the OSS equations, it is clearly feasible to directly evaluate the matrix exponential or to invert the relevant matrix. In the global approach, it is in general difficult, and in some cases impossible, to build the discretized system matrix. One possible remedy is to compute a set of global eigenmodes with iterative methods and project the flow system onto the subspace spanned by these eigenvectors. The optimization is then performed in a low dimensional model of the flow: results for the flat-plate boundary layer can be found in Ehrenstein & Gallaire (2005) and Åkervik *et al.* (2008), whereas two-dimensional and three-dimensional studies on separated flows were performed by Åkervik *et al.* (2007), Gallaire, Marquillie & Ehrenstein (2007), Ehrenstein & Gallaire (2008), Marquet *et al.* (2008), Marquet *et al.* (2009) and Alizard, Cherubini & Robinet (2009).

However, the direct *matrix-free* approach followed here is preferable, if not indispensable, for more complicated flows. This amounts to solving eigenvalue problems using only direct numerical simulations (DNSs) of the evolution operators. This approach is commonly referred to as a time-stepper technique (Tuckerman & Barkley 2000); one of its first applications was to the linear stability analysis of a spherical Couette flow (Marcus & Tuckerman 1987*a*,*b*; Mamun & Tuckerman 1995). The time-stepper technique was then generalized to optimal growth calculations by introducing the adjoint evolution operator and solving the eigenvalue problem of the composite operator (Blackburn, Barkley & Sherwin 2008; Barkley, Blackburn & Sherwin 2008) for backward-facing step flow; it was subsequently applied to the flat-plate boundary-layer flow subject to two-dimensional disturbances of Bagheri *et al.* (2009*a*).

Thus, in this paper we study the stability of the flat-plate boundary-layer flow subject to three-dimensional disturbances from a global perspective using a time-stepper technique. The base flow has two inhomogeneous directions, namely the wall-normal and streamwise, thereby allowing a decoupling of Fourier modes in the spanwise direction only. Both optimal initial condition and optimal forcing are therefore first considered for a range of spanwise wavenumbers, seeking to find the spanwise scale of the most amplified disturbances. In the case of optimal initial conditions, we optimize over a range of final times, whereas time-periodic optimal forcing is computed for a range of frequencies. In addition, we compute for the first time optimal initial conditions localized in space. The evolution of the resulting wave packet is analysed in terms of flow structures and propagation speed.

https://doi.org/10.1017/S0022112009993703 Published online by Cambridge University Press

Whereas the computation of optimal initial condition is known in the global time-stepper context (see references above), the formulation of the optimal forcing problem in this framework is novel. This enables us to compute the pseudo-spectrum of the non-normal governing operator with a matrix-free method. The latter type of analysis can have direct implications for flow control as well: The optimization procedure allows us to determine the location and frequency of the forcing to which the flow under consideration is most sensitive.

The paper is organized as follows. Section 2 is devoted to the description of the base flow and the governing linearized equations. Sections 3 and 4 describe the Lagrange approach to solving the optimization problems defined by the optimal initial conditions and optimal forcing, respectively. The main results are presented in § 5; the paper ends with a summary of the main findings.

2. Basic steady flow, governing equations and adjoint system

We investigate the stability of the classical spatially evolving two-dimensional flat-plate boundary-layer flow subject to three-dimensional disturbances. The computational domain starts at a distance x from the leading edge defined by the Reynolds number $Re_x = U_\infty x/\nu = 3.38 \cdot 10^5$ or $Re_{\delta^*} = 1.72\sqrt{Re_x} = U_\infty \delta_0^*/\nu = 10^3$. Here U_∞ is the uniform free stream velocity, δ^* is the local displacement thickness and ν is the kinematic viscosity. We denote the displacement thickness at the inflow position by δ_0^*. All variables are non-dimensionalized by U_∞ and δ_0^*. We solve the linearized Navier–Stokes equations using a spectral DNS code described by Chevalier *et al.* (2007) on a domain $\Omega = [0, L_x] \times [0, L_y] \times [0, L_z]$. The non-dimensional height of the computational box is $L_y = 30$ and the length is $L_x = 1000$, and the spanwise width is $L_z = 502.6$ for the case of localized initial conditions or defined in each simulation by the Fourier mode under investigation. In the wall-normal direction y, a Chebyshev-tau technique with $n_y = 101$ polynomials is used along with homogeneous Dirichlet conditions at the wall and the free-stream boundary. In the streamwise and spanwise directions, we assume periodic behaviour, hence allowing for a Fourier transformation of all variables. For the simulations presented here, the continuous variables are approximated by $n_x = 768$ and $n_z = 128$ Fourier modes in the streamwise and spanwise directions, respectively, whereas we solve for each wavenumber separately in the spanwise direction when considering spanwise periodic disturbances, a decoupling justified by the spanwise homogeneity of the base flow. Because the boundary-layer flow is spatially evolving, a fringe region technique is used to ensure that the flow is forced back to the laminar inflow profile at $x = 0$ (Nordström, Nordin & Henningson 1999). The fringe forcing quenches the incoming perturbations and is active at the downstream end of the computational domain, $x \in [800, 1000]$, so that $x = 800$ can be considered as the effective outflow location, corresponding to $Re_x = 1.138 \times 10^6$. The steady state used in the linearization is obtained by marching the nonlinear Navier–Stokes equations in time until the norm of the time derivative of the solution is numerically zero. Thus, the two-dimensional steady state with velocities $\boldsymbol{U} = (U(x, y), V(x, y), 0)^{\mathrm{T}}$ and pressure $\Pi(x, y)$ differs slightly from the well-known Blasius similarity solution.

2.1. *The linearized Navier–Stokes equations*

The stability characteristics of the base flow $\boldsymbol{U} = (U(x, y), V(x, y), 0)^{\mathrm{T}}$ to small perturbations $\boldsymbol{u} = (u(\boldsymbol{x}, t), v(\boldsymbol{x}, t), w(\boldsymbol{x}, t))^{\mathrm{T}}$ are determined by the linearized

https://doi.org/10.1017/S0022112009993703 Published online by Cambridge University Press

Navier–Stokes equations

$$\partial_t \boldsymbol{u} + (\boldsymbol{U}\cdot\nabla)\,\boldsymbol{u} + (\boldsymbol{u}\cdot\nabla)\,\boldsymbol{U} = -\nabla\pi + Re^{-1}\Delta\boldsymbol{u} + \boldsymbol{g}, \tag{2.1}$$

$$\nabla\cdot\boldsymbol{u} = 0, \tag{2.2}$$

subject to initial condition $\boldsymbol{u}(\boldsymbol{x}, t=0) = \boldsymbol{u}_0(\boldsymbol{x})$. Note that we have included a divergence-free forcing term $\boldsymbol{g} = \boldsymbol{g}(\boldsymbol{x}, t)$ to enable us to also study the response to forcing as well as to initial condition. In the expression above, the fringe forcing term is omitted for simplicity (see Bagheri, Brandt & Henningson 2009*b*).

When performing a systematic analysis of the linearized Navier–Stokes equations, we are interested in the initial condition $\boldsymbol{u}(0)$ and in the features of the flow states $\boldsymbol{u}(t)$ at times $t > 0$. We will also consider the spatial structure of the time-periodic forcing $\boldsymbol{g}$ that creates the largest response at large times, that is when all transients effects have died out. Our analysis will therefore consider flow states induced by forcing or initial conditions, where a flow state is defined by the three-dimensional velocity vector field throughout the computational domain Ω at time t. To this end, it is preferable to rewrite the equations in a more compact form. In order to do so, we define the velocities as our state variable, i.e. $\boldsymbol{u} = (u, v, w)^{\mathrm{T}}$. Following Kreiss, Lundbladh & Henningson (1994), the pressure can be formally written in terms of the velocity field $\pi = \mathscr{K}\boldsymbol{u}$, the solution to the equation

$$\Delta\pi = -\nabla\cdot((\boldsymbol{U}\cdot\nabla)\boldsymbol{u} + (\boldsymbol{u}\cdot\nabla)\boldsymbol{U}). \tag{2.3}$$

The resulting state space formulation of (2.1) reads

$$(\partial_t - \mathscr{A})\boldsymbol{u} - \boldsymbol{g} = 0, \quad \boldsymbol{u}(0) = \boldsymbol{u}_0. \tag{2.4}$$

Alternatively, $\mathscr{A}$ may also be defined using semi-group theory, in which it is referred to as the infinitesimal generator of the evolution operator $\mathscr{T}(t)$ (Trefethen & Embree 2005), where $\mathscr{T}$ is defined as the operator that maps a solution at time t_0 to time $t_0 + t$

$$\boldsymbol{u}(t + t_0) = \mathscr{T}(t)\boldsymbol{u}(t_0). \tag{2.5}$$

In what follows we use the evolution operator $\mathscr{T}$ to study both the response to initial condition and the regime response to forcing, i.e. we look at the long-term periodic response. Indeed, for practical numerical calculations, the variables are often discretized, so that the governing operator becomes a matrix of size $n \times n$, with $n = 3n_x n_y n_z$ for general three-dimensional disturbances. When considering spanwise periodic disturbances, we can focus on one wavenumber at a time and the dimension of the system matrix is reduced to $n = 3n_x n_y$. However, even in this case the evaluation of the discretized evolution operator $\mathscr{T} = \exp(\mathscr{A}t)$ is computationally not feasible. The complete stability analysis, including the optimization, can be efficiently performed by marching in time the linearized Navier–Stokes equations using a numerical code. This so-called time-stepper technique has indeed become increasingly popular in stability analysis (Tuckerman & Barkley 2000).

2.2. *Choice of norm and the adjoint equations*

In order to measure the departure from the base flow, we use the kinetic energy of the perturbations

$$\|\boldsymbol{u}(t)\|^2 = (\boldsymbol{u}(t), \boldsymbol{u}(t)) = \int_\Omega \boldsymbol{u}^H\boldsymbol{u}\ \mathrm{d}\Omega. \tag{2.6}$$

Because the transition in shear flows is initiated by secondary instabilities induced by local gradients in the flow, one could alternatively use an infinity norm or maximize

https://doi.org/10.1017/S0022112009993703 Published online by Cambridge University Press

directly the shear or vorticity. Using the above inner product, we may define the action of the adjoint evolution operator as

$$(\boldsymbol{v}, \exp(\mathscr{A}t)\boldsymbol{u}) = (\exp(\mathscr{A}^\dagger t)\boldsymbol{v}, \boldsymbol{u}), \tag{2.7}$$

where $\mathscr{A}^\dagger$ is defined by the initial value problem

$$-\partial_t \boldsymbol{v} = \mathscr{A}^\dagger \boldsymbol{v} = (\boldsymbol{U}\cdot\nabla)\boldsymbol{v} - (\nabla \boldsymbol{U})^{\mathrm{T}}\boldsymbol{v} + Re^{-1}\Delta \boldsymbol{v} + \nabla \mathscr{Z}\boldsymbol{v}, \quad \boldsymbol{v}(T) = \boldsymbol{v}_T. \tag{2.8}$$

The adjoint system (2.8) is derived using the inner product in time space domain $\Sigma = [0, T]\times\Omega$. The operator $\mathscr{Z}$ is the counterpart of the operator $\mathscr{K}$ for the adjoint pressure: $\sigma = \mathscr{Z}\boldsymbol{v}$. This initial value problem has a stable integration direction backwards in time, so we may define the adjoint solution at time $T-t$ for the forward running time t as

$$\boldsymbol{v}(T-t) = \exp(\mathscr{A}^\dagger t)\boldsymbol{v}_T, \quad t\in[0, T]. \tag{2.9}$$

It is important to note that the addition of the forcing term $\boldsymbol{g}$ in (2.1) has no effect on the derivation of the adjoint equations. In particular, the fringe forcing term is self-adjoint because it is proportional to the velocity $\boldsymbol{u}$.

3. Optimal initial conditions

In this section, we derive the system whose solution yields initial conditions that optimally excite flow disturbances. When seeking the optimal initial condition, we assume that the forcing term $\boldsymbol{g}$ in (2.4) is zero. We wish to determine the unit norm initial condition $\boldsymbol{u}(0)$ yielding the maximum possible energy $(\boldsymbol{u}(T), \boldsymbol{u}(T))$ at a prescribed time T. A common way of obtaining the optimal initial condition is to recognize that the condition

$$G(t) = \max_{\|\boldsymbol{u}(0)\|\neq 0} \frac{\|\boldsymbol{u}(T)\|^2}{\|\boldsymbol{u}(0)\|^2} = \max_{\|\boldsymbol{u}(0)\|\neq 0} \frac{(\boldsymbol{u}(0), \exp(\mathscr{A}^\dagger T)\exp(\mathscr{A}T)\boldsymbol{u}(0))}{(\boldsymbol{u}(0), \boldsymbol{u}(0))} \tag{3.1}$$

defines the Rayleigh quotient of the composite operator $\exp(\mathscr{A}^\dagger T)\exp(\mathscr{A}T)$. The optimization problem to be solved is hence the eigenvalue problem

$$\gamma\, \boldsymbol{u}(0) = \exp(\mathscr{A}^\dagger T)\exp(\mathscr{A}T)\boldsymbol{u}(0). \tag{3.2}$$

In the case of a large system matrix, as in fluid-flow systems, this eigenvalue problem can be efficiently solved by matrix-free methods using a time-stepper (DNS) and performing power iterations or the more advanced Arnoldi method (cf. Nayar & Ortega 1993; Lehoucq, Sorensen & Yang 1997); both methods only need a random initial guess for $\boldsymbol{u}(0)$ and a numerical solver to determine the action of $\exp(\mathscr{A}T)$ and $\exp(\mathscr{A}^\dagger T)$ (Barkley *et al.* 2008).

One alternative approach relies on the Lagrange multiplier technique, which we believe allows for more flexibility in defining different objective functions as well as in enforcing additional constrains. Here, we show how this approach is used to compute the unit norm initial condition $\boldsymbol{u}(0)$ non-zero only within a fixed region in space, $\Lambda\subset\Omega$, i.e. the localized optimal initial condition. The objective is still maximizing the kinetic energy at final time T

$$\mathscr{J} = (\boldsymbol{u}(T), \boldsymbol{u}(T)). \tag{3.3}$$

The following constraints need to be enforced: the flow needs to satisfy the governing linearized Navier–Stokes equations (2.4) (without forcing) and the initial condition

https://doi.org/10.1017/S0022112009993703 Published online by Cambridge University Press

must have unit norm and exist only inside Λ. Additionally, the optimal perturbation must be divergence-free. Hence, the Lagrange function reads

$$\mathscr{L}(\boldsymbol{u}, \boldsymbol{v}, \gamma) = (\boldsymbol{u}(T), \boldsymbol{u}(T)) - \int_0^T (\boldsymbol{v}, (\partial_t - \mathscr{A})\,\boldsymbol{u})\,\mathrm{d}\tau \\ - \gamma\,((\boldsymbol{u}(0), \boldsymbol{u}(0))_\Lambda - 1) - (\psi, \nabla\cdot\boldsymbol{u}(0))_\Lambda, \quad (3.4)$$

where $\boldsymbol{v}, \gamma$ and ψ are the Lagrange multipliers. The inner product defined by $(\cdot,\cdot)_\Lambda$ corresponds to an integral in Λ. Note that the normalization condition selects a unique solution to the eigenvalue problem and thus enables the numerical procedure to converge. We need to determine $\boldsymbol{u}, \boldsymbol{u}(0), \boldsymbol{u}(T), \boldsymbol{v}$ and γ such that $\mathscr{L}$ is stationary, a necessary condition for first-order optimality. This can be achieved by requiring that the variation of $\mathscr{L}$ is zero,

$$\delta\mathscr{L} = \left(\frac{\partial\mathscr{L}}{\partial\boldsymbol{u}}, \delta\boldsymbol{u}\right) + \left(\frac{\partial\mathscr{L}}{\partial\boldsymbol{v}}, \delta\boldsymbol{v}\right) + \left(\frac{\partial\mathscr{L}}{\partial\gamma}\right)\delta\gamma + \left(\frac{\partial\mathscr{L}}{\partial\psi}\right)\delta\psi = 0. \quad (3.5)$$

This is only fulfilled when all terms are zero simultaneously. The variation with respect to the costate variable (or adjoint state variable) yields directly the state equation

$$(\partial_t - \mathscr{A})\boldsymbol{u} = 0, \quad (3.6)$$

and similarly the variation with respect to multiplier γ yields a normalization criterion

$$\left(\frac{\partial\mathscr{L}}{\partial\gamma}, \delta\gamma\right) \Rightarrow (\boldsymbol{u}(0), \boldsymbol{u}(0))_\Lambda = 1. \quad (3.7)$$

In order to take the variations with respect to the other variables, we perform integration by parts on the second term of $\mathscr{L}$ in (3.4) to obtain

$$\mathscr{L} = (\boldsymbol{u}(T), \boldsymbol{u}(T)) - \int_0^T \left(\boldsymbol{u}, (-\partial_t - \mathscr{A}^\dagger)\,\boldsymbol{v}\right)\mathrm{d}\tau - (\boldsymbol{v}(T), \boldsymbol{u}(T)) \\ + (\boldsymbol{v}(0), \boldsymbol{u}(0)) - \gamma\,((\boldsymbol{u}(0), \boldsymbol{u}(0))_\Lambda - 1) - (\psi, \nabla\cdot\boldsymbol{u}(0))_\Lambda. \quad (3.8)$$

The variation of this expression with respect to the state variable $\boldsymbol{u}$ yields an equation for the adjoint variable as well as two optimality conditions

$$\left(\frac{\partial\mathscr{L}}{\partial\boldsymbol{u}}, \delta\boldsymbol{u}\right) \Rightarrow -\int_0^T (\delta\boldsymbol{u}, (-\partial_t - \mathscr{A}^\dagger)\boldsymbol{v}) + (\delta\boldsymbol{u}, \boldsymbol{v} - \gamma\boldsymbol{u})|_{t=0} + (\delta\boldsymbol{u}, \boldsymbol{u} - \boldsymbol{v})|_{t=T} = 0. \quad (3.9)$$

The simplest choice to satisfy this condition is that each of these terms is zero separately

$$(-\partial_t - \mathscr{A}^\dagger)\boldsymbol{v} = 0, \quad (3.10)$$

and

$$\left.\begin{aligned} \boldsymbol{u}(0) &= \gamma^{-1}\boldsymbol{v}(0), \\ \boldsymbol{v}(T) &= \boldsymbol{u}(T). \end{aligned}\right\} \quad (3.11)$$

Variations with respect to the initial velocity field give the following condition:

$$(\delta\boldsymbol{u}(0), \boldsymbol{v}(0)) - \gamma(\delta\boldsymbol{u}(0), \boldsymbol{u}(0))_\Lambda - (\delta\boldsymbol{u}(0), \nabla\psi)_\Lambda = 0. \quad (3.12)$$

The above expression can be rewritten in integral form

$$\int_{\Omega-\Lambda} (\delta\boldsymbol{u}(0)^{\mathrm{T}}\boldsymbol{v}(0)) + \int_\Lambda \delta\boldsymbol{u}(0)^{\mathrm{T}}(\boldsymbol{v}(0) - \gamma\boldsymbol{u}(0) - \nabla\psi) = 0. \quad (3.13)$$

https://doi.org/10.1017/S0022112009993703 Published online by Cambridge University Press

The first integral is zero for $\delta \boldsymbol{u}(0) = 0$, which implies that the initial condition is not updated outside Λ. Therefore, the new guess for the localized initial condition $\boldsymbol{u}(0)$ is

$$\boldsymbol{u}(0) = \gamma^{-1}(\boldsymbol{v}(0) - \nabla\psi)|_{\Lambda}. \tag{3.14}$$

In the above, the scalar field ψ is obtained by combining (3.14) with

$$\frac{\partial \mathscr{L}}{\partial \psi} = \nabla \cdot \boldsymbol{u}(0) = 0. \tag{3.15}$$

This gives a projection to a divergence-free space where the pressure-like scalar field ψ is solution to a Poisson equation. It can be proved that this is a unique projection. In our numerical implementation, the projection is actually performed by transforming in the velocity–vorticity formulation adopted for the computations (Chevalier *et al.* 2007).

The procedure described above solves an eigenvalue problem similar to (3.2) with the addition of an operator $\mathscr{PC}$ that localizes in space and projects to a divergence-free space

$$\gamma\, \boldsymbol{u}(0) = \mathscr{PC} \exp(\mathscr{A}^{\dagger} T) \exp(\mathscr{A} T) \boldsymbol{u}(0). \tag{3.16}$$

The optimality system to be solved is hence composed of (3.6), (3.7), (3.10) and (3.11) along with the projection to divergence-free space (3.14). From (3.7) and the first relation in (3.11), it can be readily seen that $\gamma = (\boldsymbol{v}(0), \boldsymbol{v}(0))$. The remaining equations are solved iteratively as follows.

Starting with an initial guess $\boldsymbol{u}(0)^n$:

(i) we integrate (3.6) forward in time and obtain $\boldsymbol{u}(T)$;

(ii) $\boldsymbol{v}(T) = \boldsymbol{u}(T)$ is used as an initial condition at $t = T$ for the adjoint system (3.10), which if integrated backward in time gives $\boldsymbol{v}(0)$;

(iii) we determine a new initial guess by localizing $\boldsymbol{v}(0)$, casting it to a divergence-free space and normalizing it to unit norm, $\boldsymbol{u}(0) = \gamma^{-1}(\boldsymbol{v}(0) - \nabla\psi)|_{\Lambda}$;

(iv) if $|\boldsymbol{u}(0)^{n+1} - \boldsymbol{u}(0)^n|$ is larger than a given tolerance, the procedure is repeated.

Before convergence is obtained, $\boldsymbol{u}(0)$ and $\boldsymbol{v}(0)$ are not aligned. At convergence, $\boldsymbol{u}(0)$ is an eigenfunction of (3.16). The iteration scheme above can be seen as a power iteration scheme finding the largest eigenvalue of the problem (3.16). Because the composite operator is symmetric, its eigenvalues are real and its eigenvectors form an orthogonal basis. The eigenvalues of the system rank the set of optimal initial conditions according to the output energy at time T. If several optimals are sought, e.g. to build a reduced order model of the flow, the sequence of $\boldsymbol{u}(0)^n$ produced in the iteration can be used to build a Krylov subspace suitable for the Arnoldi method.

4. Optimal forcing

This section focuses on the regime response of the system to time-periodic forcing. Thus, we assume zero initial conditions, $\boldsymbol{u}(0) = 0$, and periodic behaviour of the forcing function, i.e.

$$\boldsymbol{g} = \Re\left(\boldsymbol{f}(\boldsymbol{x}) \exp(\mathrm{i}\omega t)\right), \quad \boldsymbol{f} \in \mathbb{C}, \quad \omega \in \mathbb{R}, \tag{4.1}$$

where $\boldsymbol{f}$ defines the spatial structure of the forcing, ω is its circular frequency and $\Re$ denotes the real part. With these assumptions, the governing equations become

$$(\partial_t - \mathscr{A})\boldsymbol{u} - \Re\left(\boldsymbol{f} \exp(\mathrm{i}\omega t)\right) = 0, \quad \boldsymbol{u}(0) = 0. \tag{4.2}$$

In this case, we wish to determine the spatial structure and relative strength of the components of the forcing $\boldsymbol{f}$ that maximize the response of the flow at the frequency

https://doi.org/10.1017/S0022112009993703 Published online by Cambridge University Press

ω in the limit of large times, i.e. the regime response of the flow. The measure of the optimum is also based on the energy norm. Note that for this method to converge and for the regime response to be observed, the operator $\mathscr{A}$ must be globally stable. In the spatial framework, this requirement is always satisfied.

In order to formulate the optimization problem, it is convenient to work in the frequency domain, thereby removing the time dependence. By assuming time-periodic behaviour, $\boldsymbol{u}$ is replaced by the complex field $\tilde{\boldsymbol{u}}$ so that

$$\boldsymbol{u} = \Re\left(\tilde{\boldsymbol{u}} \exp(\mathrm{i}\omega t)\right). \tag{4.3}$$

The resulting governing equations can then be written as

$$(\mathrm{i}\omega\mathscr{I} - \mathscr{A})\tilde{\boldsymbol{u}} - \boldsymbol{f} = 0. \tag{4.4}$$

Note that the operator $\mathscr{A}$, containing only spatial derivatives, remains unchanged. The Lagrange function for the present optimization problem is similar in structure to that used to determine the optimal initial condition and is formulated as follows:

$$\mathscr{L}(\tilde{\boldsymbol{u}}, \tilde{\boldsymbol{v}}, \gamma, \boldsymbol{f}) = (\tilde{\boldsymbol{u}}, \tilde{\boldsymbol{u}}) - (\tilde{\boldsymbol{v}}, (\mathrm{i}\omega\mathscr{I} - \mathscr{A})\tilde{\boldsymbol{u}} - \boldsymbol{f}) - \gamma\left((\boldsymbol{f}, \boldsymbol{f}) - 1\right). \tag{4.5}$$

The objective function is the disturbance kinetic energy of the regime response $(\tilde{\boldsymbol{u}}, \tilde{\boldsymbol{u}})$, where the complex variable $\tilde{\boldsymbol{u}}$ requires the use of the Hermitian transpose. The additional constrains require the flow to be the solution to the linearized forced Navier–Stokes equations and introduce a normalization condition for the forcing amplitude. Because the state variable $\tilde{\boldsymbol{u}}$ is a solution to the time-independent system (4.4), the inner product used in the definition of the adjoint involves only spatial integrals. The time behaviour of the costate or adjoint variable is also assumed to be periodic $\boldsymbol{v} = \Re(\tilde{\boldsymbol{v}} \exp(\mathrm{i}\omega t))$. Thus, in the derivation of the adjoint, the time derivative is replaced by the term $\mathrm{i}\omega\tilde{\boldsymbol{u}}$, with adjoint $-\mathrm{i}\omega\tilde{\boldsymbol{v}}$. As for the computation of the optimal initial condition, we take variations with respect to $\tilde{\boldsymbol{u}}$, $\tilde{\boldsymbol{v}}$, $\boldsymbol{f}$ and γ:

$$\delta\mathscr{L} = \left(\frac{\partial\mathscr{L}}{\partial\tilde{\boldsymbol{u}}}, \delta\tilde{\boldsymbol{u}}\right) + \left(\frac{\partial\mathscr{L}}{\partial\tilde{\boldsymbol{v}}}, \delta\tilde{\boldsymbol{v}}\right) + \left(\frac{\partial\mathscr{L}}{\partial\boldsymbol{f}}, \delta\boldsymbol{f}\right) + \left(\frac{\partial\mathscr{L}}{\partial\gamma}\right)\delta\gamma. \tag{4.6}$$

The first-order optimality condition requires all of the terms to be simultaneously zero. By taking variations with respect to the costate variable (or adjoint variable), we again obtain the state equation (4.4). Similarly, the variation with respect to the multiplier γ yields the normalization criterion $(\boldsymbol{f}, \boldsymbol{f}) - 1 = 0$. In order to take the variations with respect to the other variables, we perform integration by parts on the second term of $\mathscr{L}$ in (4.5) to obtain

$$\mathscr{L}(\tilde{\boldsymbol{u}}, \tilde{\boldsymbol{v}}, \gamma, \boldsymbol{f}) = (\tilde{\boldsymbol{u}}, \tilde{\boldsymbol{u}}) - (\tilde{\boldsymbol{u}}, (-\mathrm{i}\omega\mathscr{I} - \mathscr{A}^{\dagger})\tilde{\boldsymbol{v}}) + (\boldsymbol{f}, \tilde{\boldsymbol{v}}) - \gamma\left((\boldsymbol{f}, \boldsymbol{f}) - 1\right). \tag{4.7}$$

No initial–final condition terms appear during this integration by parts because here the inner product is only in space (in contrast to the optimal initial condition). Variations with respect to the state variable $\tilde{\boldsymbol{u}}$ and to the forcing function $\boldsymbol{f}$ yield

$$\left(\frac{\partial\mathscr{L}}{\partial\tilde{\boldsymbol{u}}}\right) \Rightarrow \tilde{\boldsymbol{u}} - (-\mathrm{i}\omega\mathscr{I} - \mathscr{A}^{\dagger})\tilde{\boldsymbol{v}} = 0, \tag{4.8}$$

$$\left(\frac{\partial\mathscr{L}}{\partial\boldsymbol{f}}\right) \Rightarrow \boldsymbol{f} = \gamma^{-1}\tilde{\boldsymbol{v}}. \tag{4.9}$$

Equations (4.4) and (4.8) are the two equations that we have to solve with the time-stepper. The normalization condition $(\boldsymbol{f}, \boldsymbol{f}) = 1$ and (4.9) provide the optimality

https://doi.org/10.1017/S0022112009993703 Published online by Cambridge University Press

condition that is used to calculate the new forcing field after each iteration of the optimization loop.

Below, we show the equivalence between the Lagrange multiplier technique and the corresponding standard matrix method when the resolvent norm is considered. The formal solution to (4.2) can be written as

$$\tilde{\boldsymbol{u}} = (\mathrm{i}\omega I - \mathscr{A})^{-1}\boldsymbol{f}. \tag{4.10}$$

The corresponding solution for the adjoint system is

$$\tilde{\boldsymbol{v}} = (-\mathrm{i}\omega I - \mathscr{A}^{\dagger})^{-1}\tilde{\boldsymbol{u}}. \tag{4.11}$$

Combining the two equations above and using (4.9),

$$\boldsymbol{f} = \frac{1}{\gamma}(-\mathrm{i}\omega I - \mathscr{A}^{\dagger})^{-1}(\mathrm{i}\omega I - \mathscr{A})^{-1}\boldsymbol{f}. \tag{4.12}$$

This is a new eigenvalue problem defining the spatial structure of the optimal forcing at frequency ω that is solved iteratively; the largest eigenvalue corresponds to the square of the resolvent norm

$$\gamma = \|(\mathrm{i}\omega I - \mathscr{A})^{-1}\|^2. \tag{4.13}$$

Note that the actual implementation uses a slightly different formulation because the available time-stepper does not solve directly (4.4) and (4.8). In practice, the governing equations are integrated in time long enough that the transient behaviour related to the system operator $\mathscr{A}$ has died out. The regime response for the direct and adjoint system is extracted by performing a Fourier transform of the velocity field during one period of the forcing.

The steps of the optimization algorithm therefore are the follows:

(i) Integrate (4.2) forward in time and obtain the Fourier transform response $\tilde{\boldsymbol{u}}$ at the frequency of the forcing.

(ii) Here $\tilde{\boldsymbol{u}}$ is used as a forcing for the adjoint system.

(iii) A new forcing function is determined by normalizing $\boldsymbol{f}^{n+1} = \tilde{\boldsymbol{v}}/\gamma$.

(iv) If $|\boldsymbol{f}^{n+1} - \boldsymbol{f}^{n}|$ is larger than a given tolerance, the procedure is repeated.

We will also study localized optimal forcing; see § 5.2.2. The derivation of the optimality conditions is similar to that presented for spatially localized perturbations in § 3 and are not reported here.

A validation of the method is presented in figure 1, where the results from the present adjoint-based iteration procedure are compared with those obtained by the standard method of performing a singular value decomposition (SVD) of the resolvent of the Orr–Sommerfeld and Squire equations for the parallel Blasius flow (cf. Schmid & Henningson 2001). In figure 1(*a*), the response to forcing with spanwise wavenumber $\beta = 0$ is shown for different frequencies, whereas the response to steady forcing with streamwise wavenumber α is shown in figure 1(*b*). In the latter case, variations of the spanwise wavenumbers are considered. In both cases, excellent agreement between the two methods is observed.

5. Results

The flat-plate boundary-layer flow is globally stable, i.e. there are no eigenvalues of $\mathscr{A}$ located in the unstable half-plane. Hence, we do not expect to observe the evolution of single eigenmodes. In Åkervik *et al.* (2008), the non-modal stability of this flow subject to two-dimensional disturbances was studied by considering the

https://doi.org/10.1017/S0022112009993703 Published online by Cambridge University Press

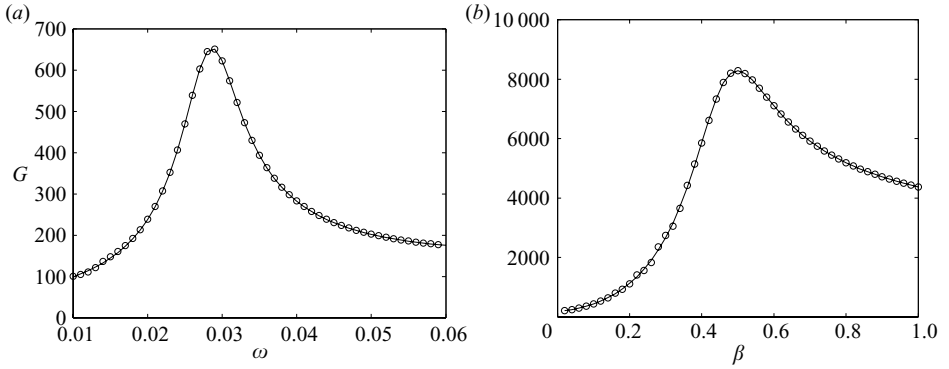


FIGURE 1. Comparison of results from the adjoint iteration scheme (circles) and direct solution in terms of SVD of the OSS resolvent (solid lines) for optimal forcing to the parallel Blasius flow at $Re = 1000$. (a) Zero spanwise wavenumber β for different frequencies ω and for streamwise wavenumber $\alpha = 0.1$. (b) Streamwise wavenumber $\alpha = 0.1$ for different spanwise wavenumbers β subject to forcing with frequency $\omega = 0.05$. Both plots show excellent agreement between the two methods. Note that in order to obtain a regime response in the parallel case, the wavenumbers are chosen so that the system operator is stable.

optimal superposition of eigenmodes. These authors found that the optimal initial condition exploits the well-known Orr mechanism to efficiently trigger the propagating TS wave packet. In Bagheri *et al.* (2009*a*), the stability of the same flow was studied using forward and adjoint iteration scheme together with the Arnoldi method to reproduce the same mechanism. By allowing for three-dimensional disturbances, it is expected that in addition to the instability mechanisms mentioned above (convective TS instability and the Reynolds stress mechanism of Orr), the lift-up mechanism will be relevant in the system.

This has been well understood both using the OSS equations (Butler & Farrell 1992; Reddy & Henningson 1993) in the parallel temporal framework and using the parabolized stability equations in the spatial non-parallel framework (Andersson *et al.* 1999; Luchini 2000; Levin & Henningson 2003). In the former formulation, the base flow is assumed to be parallel. At the Reynolds number $Re = 1000$, the inflow Reynolds number of the present investigation, it is found that for spanwise wavenumbers β larger than ≈ 0.3, there is no exponential instability of TS/oblique waves. The largest non-modal growth due to the lift-up mechanism is observed at the wavenumber pair $(\alpha, \beta) = (0, 0.7)$. In this work, we do not restrict ourselves to zero streamwise wavenumber $\alpha = 0$, but instead take into account the developing base flow. Indeed, the spatially developing base flow allows for transfer of energy between different wavenumbers through the convective terms.

5.1. *Optimal initial condition*

5.1.1. *Spanwise periodic flows*

We investigate the potential for growth of initial conditions with different spanwise wavenumbers β by solving the eigenvalue problem (3.2) for a range of instances of time T. As explained above, this amounts to performing a series of direct and adjoint numerical simulations until convergence towards the largest eigenvalues of (3.2) is obtained.

Figure 2(a) shows the energy evolution when optimizing for different times and spanwise wavenumber $\beta = 0.55$. It is at this wavenumber that the maximum growth

https://doi.org/10.1017/S0022112009993703 Published online by Cambridge University Press

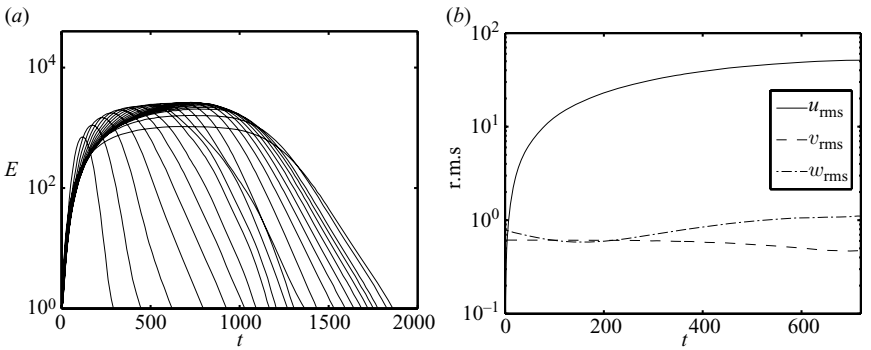


FIGURE 2. (*a*) Energy evolution of the optimal initial conditions for different times T at the wavenumber $\beta = 0.55$, where the optimal streak growth is obtained. The largest growth is obtained at time $T = 720$. The maximum at each time in this figure defines the envelope growth. (*b*) Component-wise r.m.s. values when optimizing for time $T = 720$. A transfer of energy from the wall-normal and spanwise component to the streamwise velocity is observed during the time evolution, clearly showing that the lift-up mechanism is active.

due to the lift-up mechanism is found for the configuration under consideration. From figure 2(*b*) it is evident that the disturbance leading to the maximum streak growth at time $T = 720$ exploits the component-wise transfer between velocity components inherent to the lift-up mechanism. The initial condition is in fact characterized by strong wall-normal v and spanwise w perturbation velocity while the flow at later times is perturbed in its streamwise velocity component.

An important feature of this high-Reynolds-number flat-plate boundary-layer flow with length $L_x = 800$ is that the combined Orr/Tollmien–Schlichting mechanism is very strong with a growth potential of $\gamma_1 = 2.35 \times 10^4$ (see also Bagheri *et al.* 2009*a*) for time $T = 1800$. If, however, the streaks induced by the lift-up mechanism have reached sufficiently large amplitudes to trigger significant nonlinear effects, the TS wave transition scenario will be bypassed. In figure 3, a contour map of the maximum growth versus optimization time and spanwise wavenumbers β is shown. Note that local maxima are obtained in two regions: (i) a low spanwise wavenumber regime dominated by the TS/oblique waves where the growth is the largest but slow and (ii) for high spanwise wavenumber, it is the fast lift-up mechanism that is dominating. The TS/oblique mechanism can be seen to yield one order of magnitude larger growth than the lift-up instability. The global maximum growth is obtained at the wavenumber $\beta = 0.05$ and not for $\beta = 0$. This somewhat surprising result can be explained by the larger initial transient growth of spanwise-dependent perturbations which initiates the TS-waves. The growth rate of TS-waves is almost independent of β for the low values under consideration (see e.g. figure 3.10 of Schmid & Henningson 2001).

The competition between the exponential and algebraic growth was also studied using local theory by Corbett & Bottaro (2000). These authors have shown that as the Reynolds number increases, the growth due to modal instability becomes more pronounced. The results presented in that work for $Re_\theta = 386$ (equivalent to $Re_{\delta^*} = 1000$ in our scaling) indicate that TS instability becomes dominant for final times $T > 2000$. Our results show that in a spatially evolving boundary layer with local Reynolds number Re_{δ^*} ranging between 1000 and 1800, the exponential growth dominates at times larger than about 1250. In the following, we study in

https://doi.org/10.1017/S0022112009993703 Published online by Cambridge University Press

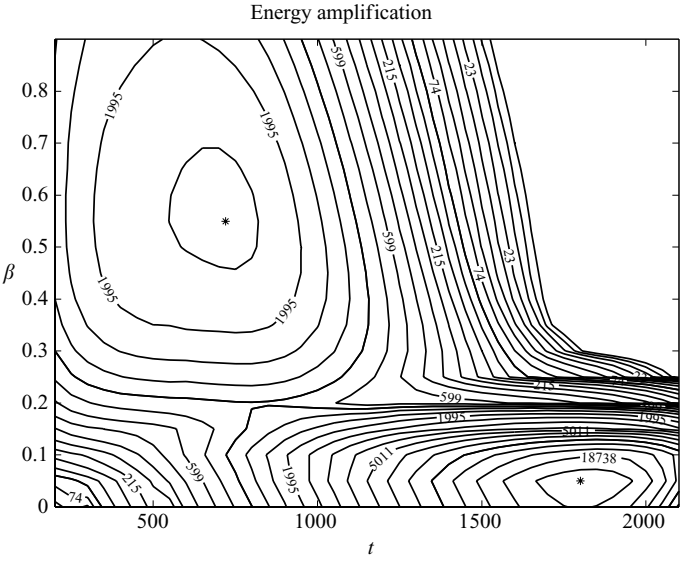


FIGURE 3. Contour map of optimal growth due to initial condition in the time spanwise wavenumber domain. The contour levels span three orders of magnitude and thus we use a logarithmic scale. The values on the contours indicate the energy growth corresponding to that line. The maximum streak growth is obtained for $\beta = 0.55$ at time $T = 720$ and the amplification factor is $G = 2.63 \times 10^3$. The global maximum is obtained for $\beta = 0.05$ at time $T = 1820$, with the streamwise exponential amplification of oblique waves combined with the Orr mechanism. The amplification factor is $G = 2.71 \times 10^4$.

more detail the disturbances corresponding to the two local maxima mentioned above.

The evolution of the most dangerous initial condition is shown in figure 4. The streamwise velocity component of the optimal initial condition leading to the maximum growth at time $T = 1820$ is depicted together with the flow response at various times. The initial disturbance is the same as in the two-dimensional case leaning against the shear of the base flow (see figure 4*a*). The resulting instability exploits the Orr mechanism to efficiently initialize the wave packet propagation, eventually giving the disturbance shown in figure 4(*b–d*).

Figure 5 shows the space–time diagram for the evolution of the three velocity components of the disturbance. Isocontours of the integrated, in the spanwise and wall-normal directions, root-mean-square (r.m.s.) values associated with each component are plotted versus the streamwise direction and time. Because this is a global view of local modal instability, there is no significant component-wise transfer of energy, and thus the different components of the disturbance evolve (grow) in a similar manner. Weak interactions between the components can be due to non-parallel effects. Additionally, the propagation velocity of the disturbance is estimated from the space–time diagrams by tracking the edges of the disturbance. These edges are defined as the point where the r.m.s. values have amplitude 1 % of the local peak value. (All the propagation velocities presented will be measured in this way.) The leading edge of the wave packet travels at $c_{le} = 0.51$ whereas the trailing edge has a velocity $c_{te} = 0.33$. These values show remarkable agreement with the classic results on the propagation of wave packets by Gaster (1975) and Gaster & Grant (1975).

https://doi.org/10.1017/S0022112009993703 Published online by Cambridge University Press

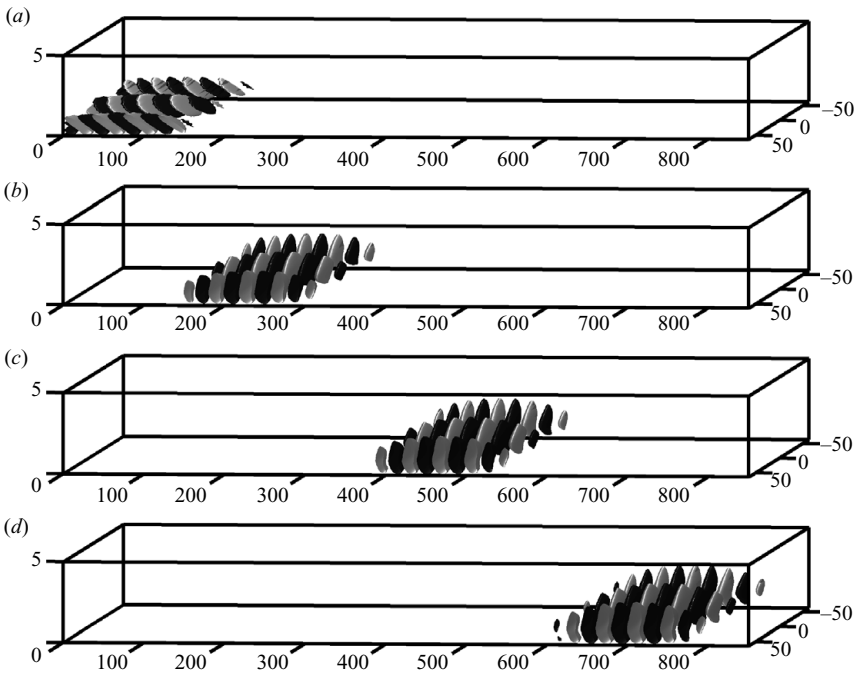


FIGURE 4. Isosurfaces of streamwise component of disturbances at the spanwise wavenumber $\beta = 0.05$. Red/blue colour signifies isosurfaces corresponding to positive/negative velocities at 10 % of the maximum. (*a*) Streamwise component of optimal initial condition leading to the global optimal growth at time $T = 1820$. (*b–d*) Corresponding flow responses at times $T = 400$, 1000 and 1600.

The optimal initial condition leading to the maximum growth at time $T = 720$ for spanwise wavenumber $\beta = 0.55$ and the corresponding flow response at various times are shown in figure 6. The initial disturbance is an elongated perturbation with most of its energy (99.94 %) in the wall-normal and spanwise velocity components (figure 6*a*). The resulting instability exploits the lift-up eventually giving the disturbance shown in figure 6(*b–e*). This is a result of local non-modal instability characterized by the strong transfer of energy from the wall-normal and spanwise towards the streamwise velocity component. The wall-normal velocity component is shown in figure 6(*b*) to suggest that the Orr mechanism is active here as well; it delays the final decay of the streamwise vortices so that they can induce streaks more effectively. Already at time $t = 100$ more than 99 % of the kinetic energy of the perturbation is in the streamwise component. As can be seen, the disturbance evolves into alternating slow and fast moving streaks that are tilted so that the leading edge is higher than the trailing edge as observed in the experimental investigation by Lundell & Alfredsson (2004).

Note that although the optimal initial condition is streamwise independent for parallel flows, it is localized in the streamwise direction for a spatially growing boundary layer. This indicates that it is most efficient to extract energy from the mean flow farther upstream where non-parallel effects are stronger. For optimization times longer than that of the peak value, still with $\beta = 0.55$, the initial perturbation is located farther upstream and is shorter. This is to compensate for the downstream propagation of perturbations out of the control domain. Conversely, for optimization times lower than $T = 720$, the initial conditions assume more and more the form of a

https://doi.org/10.1017/S0022112009993703 Published online by Cambridge University Press

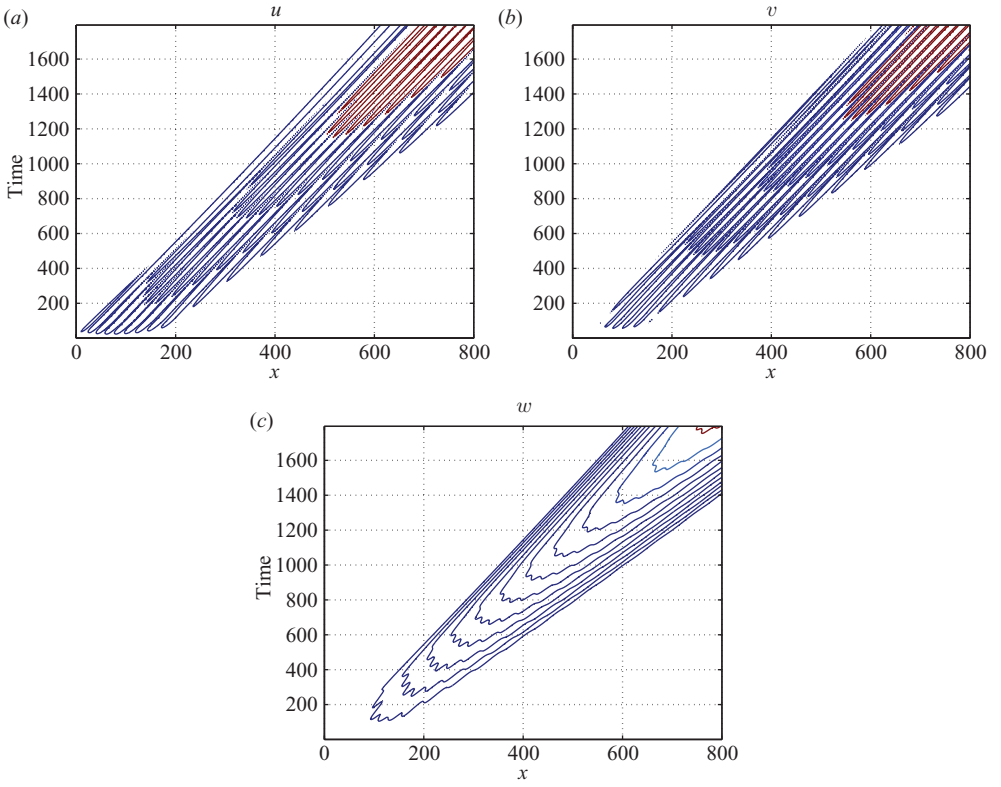


FIGURE 5. Spatio-temporal diagram of the three velocity components of the perturbation for the TS-wave case (optimization time is $T = 720$) (*a* streamwise, *b* wall normal and *c* spanwise). The propagation velocity of the leading edge of the disturbance is $c_{le} = 0.51$ whereas that of the trailing edge is $c_{te} = 0.33$.

packet of vortices aligned in the streamwise direction and tilted upstream. The growth is then due to a combined Orr and lift-up mechanism.

The space–time diagram for each velocity component of the streaky optimal perturbation is presented in figure 7. The non-modal nature of the instability and the component-wise transfer of energy are seen in the plots. The streamwise component is for large times several orders of magnitude larger than that for the other two. The propagation velocity of the disturbance is calculated: the leading-edge velocity of the 'streak-packet' is $c_{le} = 0.87$ whereas the trailing edge travels at velocity $c_{te} = 0.44$. Note that these values are based on the streamwise velocity component. The propagation velocities of the non-modal streaks are larger than those of modal disturbances. This can be explained by the fact that the disturbances are located in the upper part of the boundary layer, especially in the downstream part, as also deduced from the three-dimensional visualization in figure 6. Note, finally, in the plot for the spanwise velocity component a kink around $t = 400$ and $x = 400$. In this region, the main contribution to the trailing edge of the disturbance changes from streamwise vortices to streamwise streaks. The propagation velocity of streamwise vortices is thus larger than that of the streaks as confirmed by the reduced slope of the peak contours in figures 7(*a*) and 7(*b*).

To further interpret the present results, we perform a Fourier transform along the streamwise direction of the two disturbances investigated above and compute the

https://doi.org/10.1017/S0022112009993703 Published online by Cambridge University Press

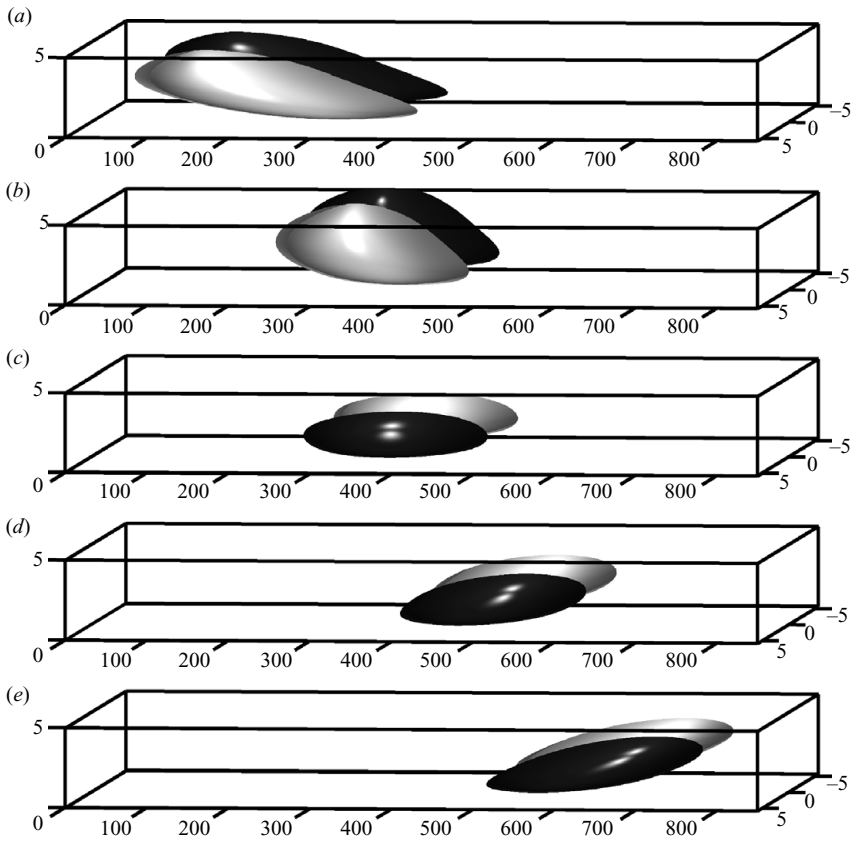


FIGURE 6. Evolution of streamwise velocity when initializing the system with the optimal initial condition at $\beta = 0.55$. (*a*) The wall-normal velocity of the optimal initial condition. (*b*) The wall-normal velocity at $t = 200$ with surface levels at 10 % of its maximum value. (*c*) The streamwise velocities at $t = 200$, (*d*) $t = 400$ and (*e*) $t = 600$. The optimization time is $T = 720$.

energy distribution in the various streamwise wavenumbers α (the energy density is first integrated in the wall-normal and spanwise directions). The result shown in figure 8 demonstrates that the TS-wave disturbance has a peak at a relatively higher $\alpha \approx 0.17$, a value in agreement with predictions from local parallel stability calculations. The streak mode, conversely, has most of its energy at the lowest wavenumbers.

Four different optimal initial conditions for $\beta = 0.55$ and $T = 720$ are shown in figure 9. The wall-normal velocity component of the eigenvector leading to the maximum growth is reported in 9(*a*). Because the base flow is uniform in the spanwise direction, the second eigenvector has the exact same shape as the first, only shifted half a wavelength in z as shown in figure 9(*b*). These eigenvectors correspond to the same eigenvalue $\gamma_{1,2} = 2.6 \times 10^3$, and they may be combined linearly to obtain a disturbance located at any spanwise position. In figure 9(*c*,*d*), the third eigenvector associated with $\gamma_3 = 2.2 \times 10^3$ and the fifth eigenvector associated with $\gamma_5 = 1.6 \times 10^3$ are shown, respectively. These eigenvectors also come in pairs with matching eigenvalues. It is thus possible by the Arnoldi method to obtain several optimals for a single parameter combination. This has not been done previously for

https://doi.org/10.1017/S0022112009993703 Published online by Cambridge University Press

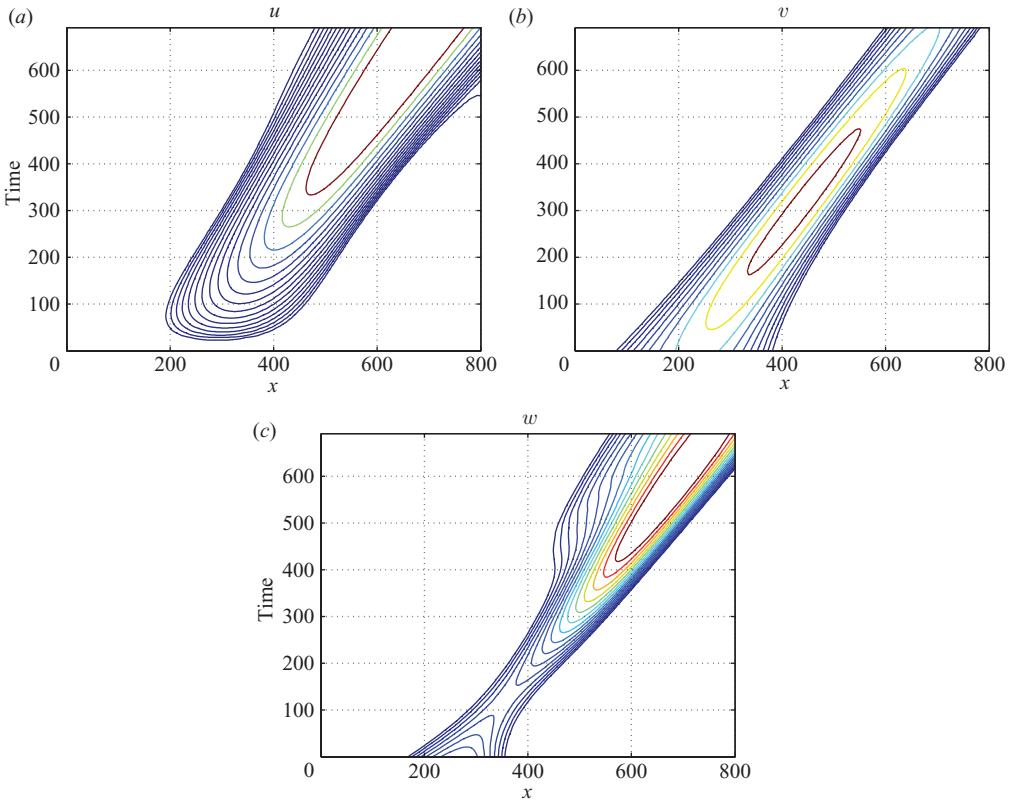


FIGURE 7. Spatio-temporal diagram of the three velocity components of the perturbation for the streak case (optimization time is $T = 720$) (*a* streamwise, *b* wall normal and *c* spanwise). The propagation velocity of the leading edge of the disturbance is $c_{le} = 0.87$ whereas that of the trailing edge is $c_{te} = 0.44$. The two speeds are measured in the second half of the time domain after the initial transient phase.

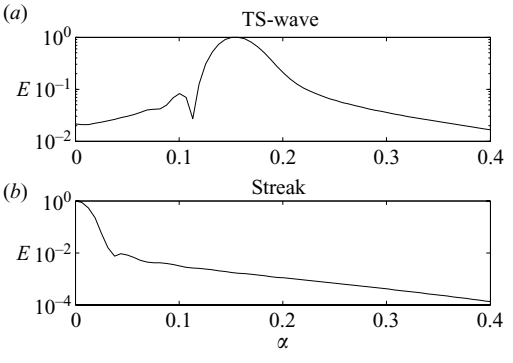


FIGURE 8. Energy spectra along the streamwise direction for the optimal initial condition at $T = 1820$, $\beta = 0.05$ (TS-wave) and $T = 720$, $\beta = 0.55$ (streak).

the Blasius flow, although Blackburn *et al.* (2008) computed several optimals for the flow past a backward-facing step.

The responses to each of these initial conditions are shown in figure 9(*e–i*). One can see that the sub-optimal initial conditions reproduce structures of shorter extension

https://doi.org/10.1017/S0022112009993703 Published online by Cambridge University Press

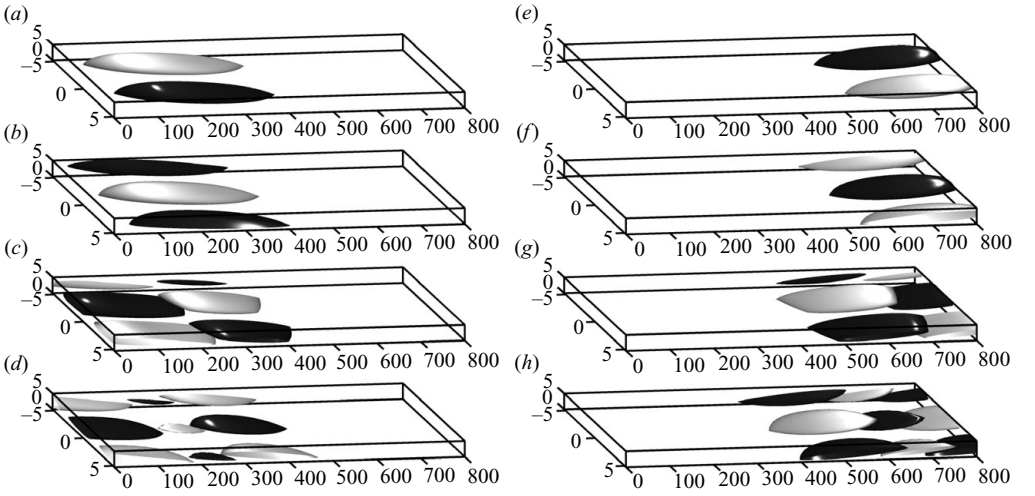


FIGURE 9. Wall-normal component of the leading four eigenvectors for the optimization problem at $\beta = 0.55$, $t = 720$ and the corresponding responses. The structures are plotted over one wavelength in the spanwise direction. Red/blue colour indicate isosurfaces corresponding to positive/negative velocities at 10 % of the maximum. (*a*) The initial condition with largest growth. (*b*) Flow structures corresponding to the second eigenvalue. This is a spanwise-shifted version of the first eigenvector. (*c*) Third eigenvector associated with the same eigenvalue as the fourth eigenvector (not shown). (*d*) Fifth eigenvector. In (*e–g*) and (*i*), the corresponding responses are shown, in particular the streamwise component. Note that the axes are not at the actual aspect ratio: the structures are far more elongated.

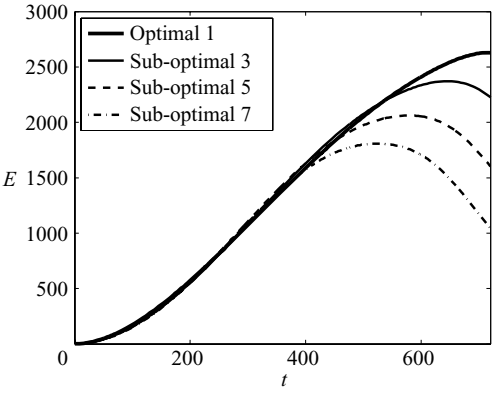


FIGURE 10. The evolution of the energy of the perturbation in time for each of the initial conditions in figure 9. The sub-optimals denoted by even number give the same evolution as the corresponding perturbation with odd number.

and with low- and high-speed streaks alternating in the streamwise direction. Figure 10 shows the energy evolution versus time for each of the sub-optimals. The energy growth is similar in the beginning; however, later on, faster decay is observed with decreasing order of optimality. Optimal perturbations form an orthogonal basis; this fact may be exploited to project incoming disturbances and predict their evolution.

5.1.2. *Localized optimal initial condition*

In this section, we look into the general case of three-dimensional initial disturbances using the method described in § 3. A large domain is chosen to allow for a fully

https://doi.org/10.1017/S0022112009993703 Published online by Cambridge University Press

Time	Component	Initial condition	Response	Total growth
	u	0.00398	275.42913	
720	v	0.36452	0.02334	275.76202
	w	0.63149	0.30954	
	u	0.74441	1012.39550	
1820	v	0.00314	278.58122	1763.75695
	w	0.25244	472.78022	

TABLE 1. Energy of each component of the tree-dimensional optimal initial condition and the corresponding response. The total energy amplification is reported in the last column. All the values are normalized with the total energy of the initial condition.

three-dimensional disturbance to propagate and expand in all directions without interacting with the boundaries. The spanwise width is chosen to be $Lz = 502.6$ (corresponding to the fundamental wavenumber $\beta = 0.0125$) for the cases with longest optimization time and $Lz = 251.3$ ($\beta = 0.025$) for the shorter optimization times. Furthermore, $n_z = 128$ Fourier modes were used in the spanwise direction, instead of four for the spanwise periodic cases. This increases the total number of degrees of freedom in our optimization problem from approximately 1–30 million.

The initial condition is placed near the inflow of the computational domain and power iterations are used to compute the optimal shape of the disturbance inside a fixed region. The area to which the initial condition is limited is $30\delta_0^*$ long and $40\delta_0^*$ wide and it is centred around the location $x = 25\delta_0^*$ and $z = 0$. Along the wall-normal direction the optimization process restricts the perturbation near the wall, inside the boundary layer, hence no additional localization is adopted. The cases presented here correspond to the two physical mechanisms found to be relevant in the previous section: the Orr/TS-wave scenario and the lift-up process. To excite the two separately, the corresponding optimization times are chosen to be $T = 1820$ and $T = 720$. In addition, one intermediate case, $T = 900$, where both these mechanisms are active, is presented.

For the longest optimization time considered (see figure 11), the TS-wave scenario completely dominates the dynamics. The characteristic upstream tilted structures are present in the initial condition and all the velocity components achieve a significant growth. The wave packet grows while travelling downstream and it consists of structures almost aligned in the spanwise direction, forming symmetric arches. The three-dimensional nature of this wave packet is noticeable in the spanwise velocity component of the response, accounting for the spreading of the disturbance normal to the propagation direction and to the presence of unstable oblique waves. As in the case of the spanwise periodic disturbances, the total energy growth due to the streamwise normality (TS-waves for $T = 1820$) is about of one order magnitude larger than the amplification triggered by the lift-up effect at $T = 720$ (component-wise non-normality). Table 1 compiles the energy amplifications for the cases under investigation and reports the value of the energy content in each velocity component for the initial and final conditions.

The flow structures shown in figure 12, with corresponding amplitudes in table 1, document the optimal initial conditions for $T = 720$. The lift-up effect with the formation of streamwise elongated streaks is evident in this case. The initial condition is characterized by strong streamwise vorticity, wall-normal and spanwise velocity components, whereas the response is predominantly in the streamwise

https://doi.org/10.1017/S0022112009993703 Published online by Cambridge University Press

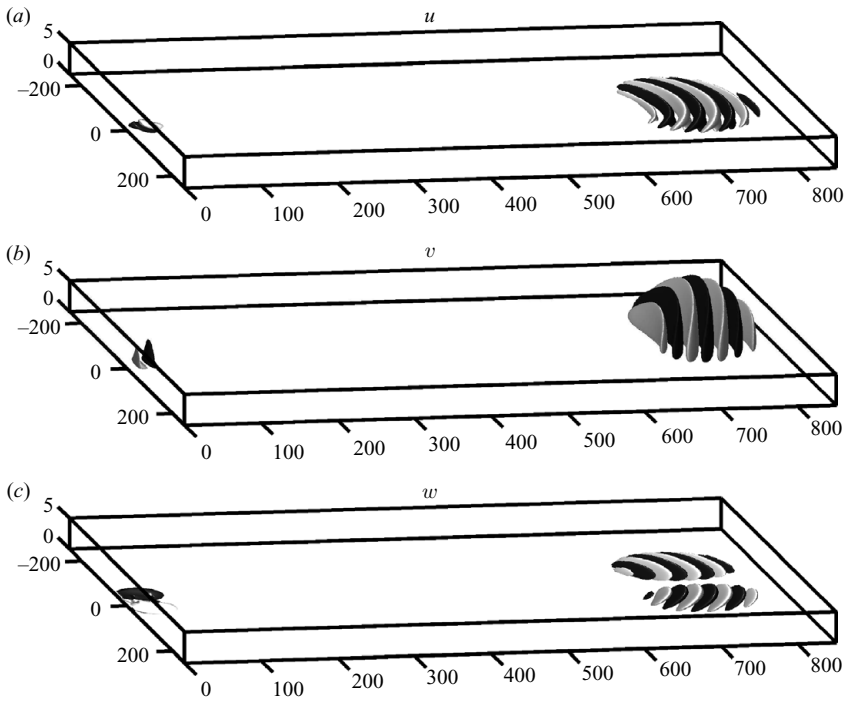


FIGURE 11. Optimal localized initial condition and corresponding response at time $T = 1820$, the optimal TS wave packet. The amplitudes of each velocity component are reported in table 1.

velocity component. Interestingly, we note weak TS-waves propagating behind the streaks (visible in the wall-normal and spanwise velocity components). Because the optimization time is short, TS-waves will not have the opportunity to grow and their contribution to the initial condition is therefore limited. However, this cannot be zero for a localized initial perturbation. Note further that the spanwise component is found to be weak and hence the spreading of the disturbance in this direction is limited.

The characteristics of the optimal wave packets are analysed by the space–time diagrams in figures 13 and 14. Here, the propagation of the disturbance in the streamwise direction is determined by considering the integral of the energy associated with each velocity component in the wall-normal and spanwise directions. Similarly, the lateral spreading is computed by integrating the perturbation velocities in the streamwise and wall-normal directions. Comparing the two cases we see that the TS wave packet expands faster in the spanwise direction while travelling downstream more slowly than the optimal streaky wave packet. The propagation velocity of the leading edge of the TS-like disturbance is $c_{le} = 0.47$ whereas the trailing edge travels at $c_{te} = 0.32$. The spanwise spreading speed is $c_z = 0.084$, corresponding to an angle of $\theta = 11.46^\circ$. These values can be compared to those observed experimentally by Gaster (1975) and Gaster & Grant (1975) and to the theoretical analysis of Koch (2002). Koch (2002) determined the propagation speed of the leading edge of a localized wave packet to be 0.5 and the trailing-edge velocity to be 0.36 by computing the group velocity of three-dimensional neutral waves. The largest spanwise group velocity was found to be approximately 0.085, a value very close to those reported here. The

https://doi.org/10.1017/S0022112009993703 Published online by Cambridge University Press

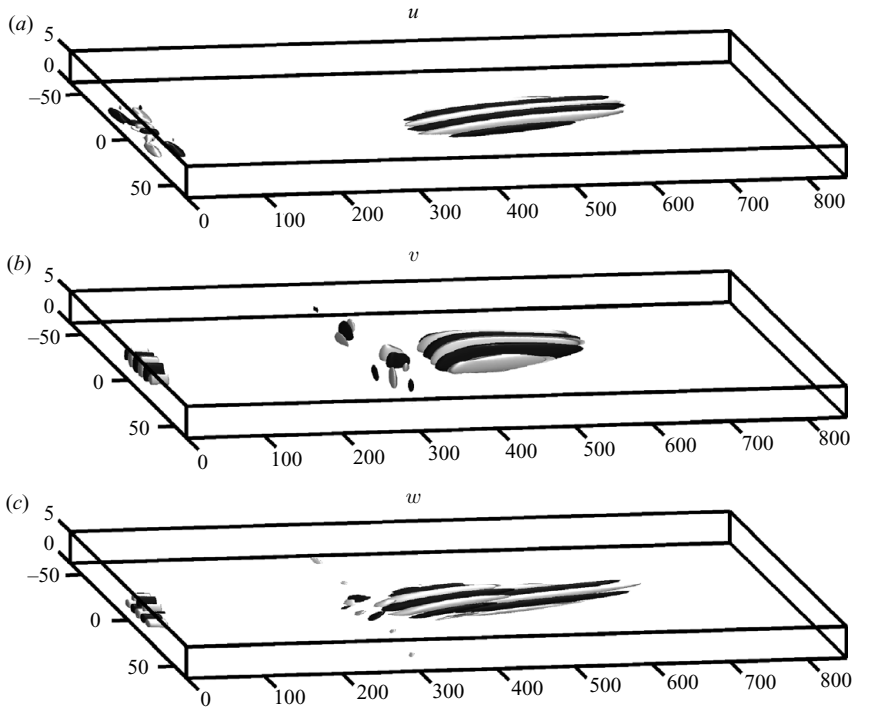


FIGURE 12. Optimal localized initial condition and corresponding response at time $T = 720$, the optimal streaky wave packet. The amplitudes of each velocity component are reported in table 1.

agreement is remarkable even though the results of Koch (2002) are obtained at a lower Reynolds number, i.e. $Re = 580$.

The difference between leading and trailing edges of the optimal streaky wave packet, $c_{le} = 0.90$ and $c_{te} = 0.36$, explains the larger extension of the latter; although the front travels at the speeds typical of the upper part of the boundary layer where the streaks are located, the trailing edge velocity is that of the unstable waves seen on the rear. The spanwise spreading speed is $c_z = 0.0098$, corresponding to an angle of $\theta = 0.89°$. This spreading rate is that of the energetically dominant velocity component, i.e. the streamwise component. The slow lateral diffusion is most likely only due to the effect of viscosity; the growing streaky structures are therefore characterized by zero spanwise propagation velocity.

Figures 14(b) and 14(c) clearly demonstrate the short and slower packet of waves following the main streaky structures. As mentioned above, the spanwise propagation of the streamwise vortices and streaks is limited; conversely, the sequence of waves on the rear part of the wave packet has a spanwise spreading rate comparable to that of the TS wave packet, in particular the value $c_z = 0.073$ is obtained by considering the energy of the spanwise velocity component.

Finally, we computed optimal disturbances for intermediate optimization times when amplifications are generally lower than those in the two previous cases. For times around $T = 800$ to $T = 900$ perturbations containing both streaky and wavy structures emerge. The spectrum of the initial conditions contains a broad range of disturbances, whereas the flow response is again characterized by short-wavelength

https://doi.org/10.1017/S0022112009993703 Published online by Cambridge University Press

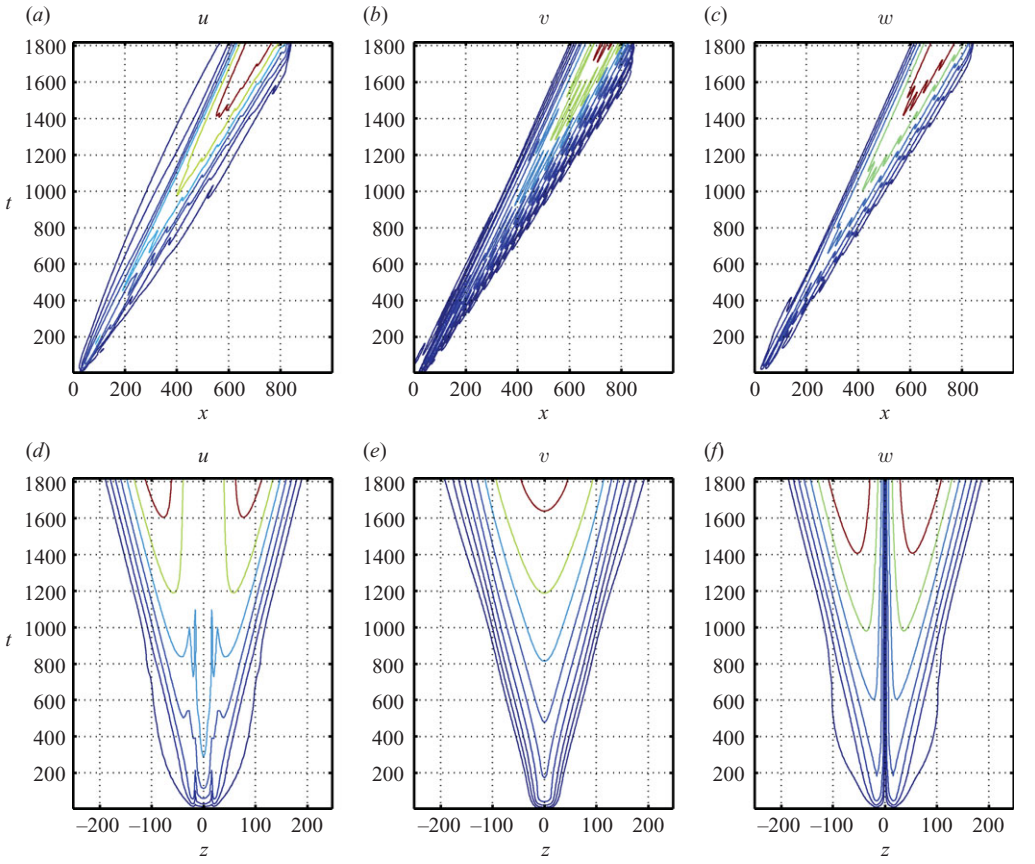


FIGURE 13. Spatio-temporal diagram of the integrated in the wall-normal direction of the r.m.s. values of three velocity components of the perturbation for the optimal TS wave-packet (optimization time $T = 1820$). (*a–c*) The spreading of the disturbance in the streamwise direction where the disturbance velocity is integrated in the spanwise and wall-normal directions: (*a*) streamwise, (*b*) wall-normal and (*c*) spanwise velocity components, respectively. (*d–f*) The evolution in the spanwise direction of the perturbations integrated in the streamwise and wall-normal directions. The propagation velocity of the leading edge of the disturbance is $c_{le} = 0.47$ whereas that of the trailing edge is $c_{te} = 0.32$. The spanwise spreading speed at sufficiently large times is $c_z = 0.084$.

instability waves following elongated streaks. The TS wave packet becomes more and more relevant as the optimization time increases.

5.2. *Optimal forcing*

5.2.1. *Global forcing*

Because boundary layers are convectively unstable, thereby acting as noise amplifiers, a prominent role is played by the response to forcing, rather than by the time evolution of the initial condition. The optimal forcing is therefore a relevant measure of the maximum possible growth that may be observed in the computational domain. Analysis of the frequency response can also have implications for control revealing the forcing location and frequencies to which the flow is most sensitive. Although the evolution of the optimal initial condition consists of the propagation

https://doi.org/10.1017/S0022112009993703 Published online by Cambridge University Press

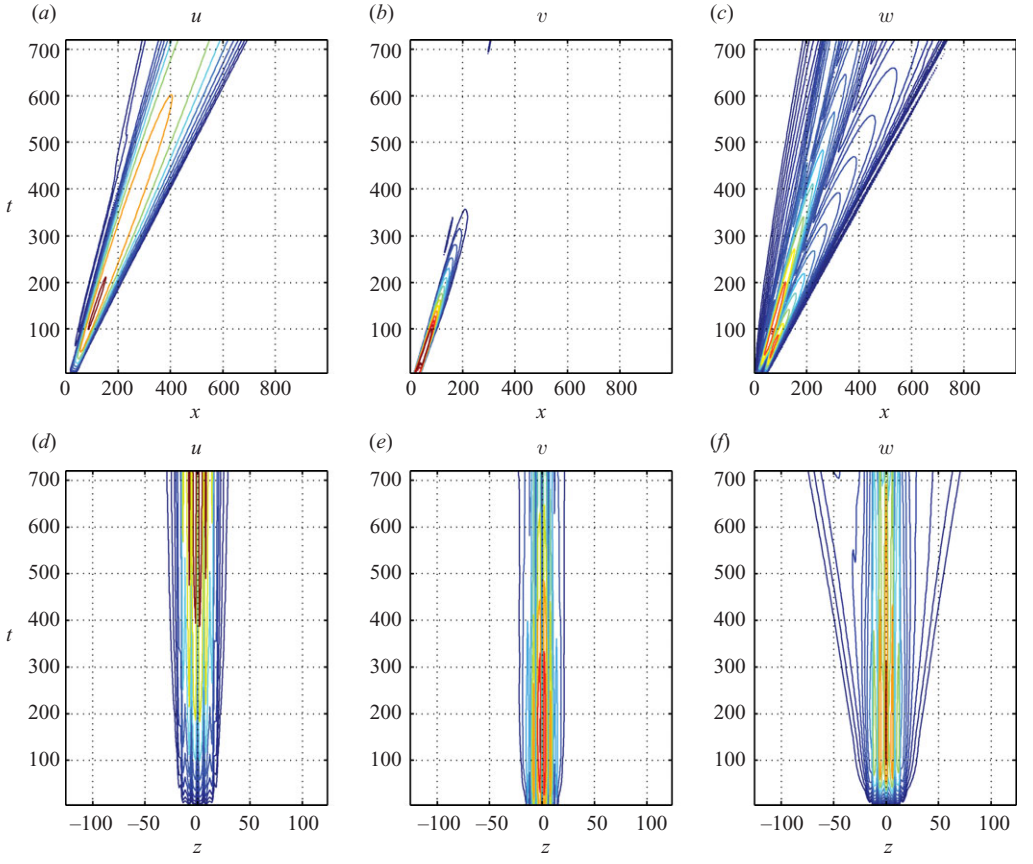


FIGURE 14. Spatio-temporal diagram of the integrated in the wall-normal direction of the r.m.s. values of three velocity components of the perturbation for the optimal streaky wave packet (optimization time $T = 720$). (*a–c*) The propagation of the disturbance in the streamwise direction where the disturbance velocity is integrated in the spanwise and wall-normal directions: (*a*) streamwise, (*b*) wall-normal and (*c*) spanwise velocity components, respectively. (*d–f*) The evolution in the spanwise direction of the perturbations integrated in the streamwise and wall-normal directions. The propagation velocity of the leading edge of the disturbance is $c_{le} = 0.90$ whereas that of the trailing edge is $c_{te} = 0.36$. The spanwise spreading speed is $c_z = 0.0098$ (based on the u component).

and amplification of a wave packet, eventually leaving the computational box (or measurement section), the response of the flow to periodic forcing will consist of structures with a fixed amplitude at each streamwise station, oscillating around the mean flow. We investigate the structure of the optimal forcing and the corresponding response for a range of spanwise wavenumbers and frequencies. Thus, for each wavenumber we examine a number of temporal frequencies. Ideally, we would like to solve the linearized Navier–Stokes equations for very large times, ensuring that we are only considering the regime (long-time) response at the specific frequency under investigation. In practice, however, we are restricted to a finite final time by the computational cost of solving the direct and adjoint equations involved in the iteration scheme. Using power iterations to find the largest eigenpair typically requires from approximately 15 iterations to about 100 for the most stable frequencies; in

https://doi.org/10.1017/S0022112009993703 Published online by Cambridge University Press

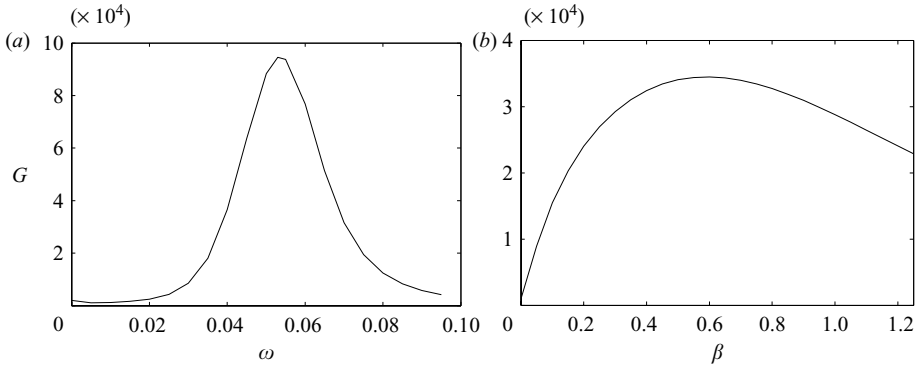


FIGURE 15. (*a*) Frequency response for zero spanwise wavenumber i.e. two-dimensional disturbances. The optimal response is obtained for the frequency $\omega = 0.055$. (*b*) Response to zero frequency forcing $\omega = 0$ for different spanwise wavenumbers. The maximum response is obtained at $\beta = 0.6$.

other words, we need to integrate the governing equations at least 30 times. As can be deduced from the results in the previous section, transiently growing perturbations of small spanwise scale leave our domain at time $t \approx 2000$, while locally unstable TS-waves propagate at a speed of about 0.3 U_∞. This observation, along with several convergence tests using different integration intervals to extract the flow regime response, leads to the conclusion that integration to $T = 5000$ is long enough to observe the pure frequency response.

Figure 15 shows the square of the resolvent norm, i.e. the response to forcing for the two limiting cases $\beta = 0$ and $\omega = 0$. In figure 15(*a*), the response to two-dimensional forcing, inducing perturbations with $\beta = 0$, is displayed. The maximum response is observed for the frequency $\omega = 0.055$. This maximum is obtained at the frequency where the least stable TS eigenvalue is located (see Bagheri *et al.* 2009*a*). Indeed, it is known that by projecting the dynamics of the flow onto the basis of eigenmodes, the response to forcing is given by the combination of resonant effects (distance in the complex plane from forcing frequency to eigenvalue) and non-modal effects, i.e. the cooperating non-orthogonal eigenvectors (Schmid & Henningson 2001). In Åkervik *et al.* (2008) it was shown for a similar flow that non-normal eigenvectors could induce a response about 20 times larger than that induced only by resonant effects.

The response to zero temporal frequency for different spanwise wavenumbers β is shown in figure 15(*b*), where according to local theory the maximum response is expected for spanwise periodic excitations. The maximum growth may be observed for the wavenumber $\beta = 0.6$, a slightly larger value than that for the optimal initial condition case. Note that in the case of optimal forcing there is a smaller difference in the maximum gain between the two different dominating mechanisms (TS-waves versus streaks).

A full parameter study has been carried out in the frequency–spanwise wavenumber (ω, β) plane. A contour map showing the regime response to optimal forcing is displayed in figure 16. As in the case of the optimal initial condition, the global maximum response to forcing is observed for $\beta = 0.05$. It reaches this maximum for the frequency $\omega = 0.055$. A second region of strong amplification is found for low frequencies and high spanwise wavenumbers. Here the most amplified structures

https://doi.org/10.1017/S0022112009993703 Published online by Cambridge University Press

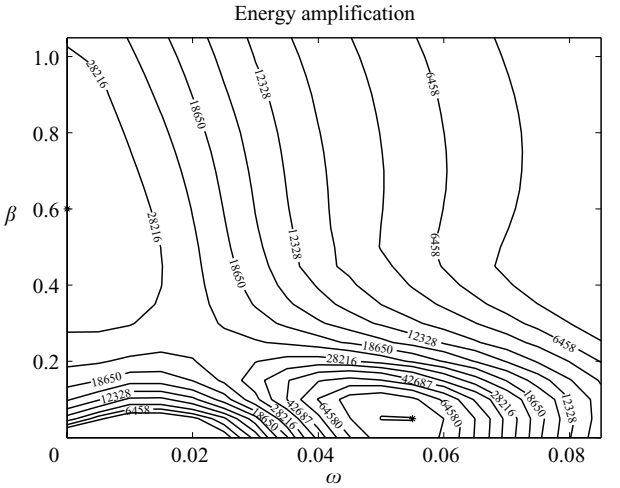


FIGURE 16. Contour map of response to forcing with frequency ω versus spanwise wavenumber β. The contour levels span three orders of magnitude and thus we use a logarithmic scale. The value on the contours indicates the energy growth corresponding to that line. The maximum response to forcing is observed for $\beta = 0.05$ and for the frequency $\omega = 0.055$. The amplification factor is $G = 1.01 \times 10^5$. The maximum growth due to the streak mechanism is found for the spanwise wavenumber $\beta = 0.6$ at $\omega = 0$ where the amplification factor is $G = 3.45 \times 10^4$.

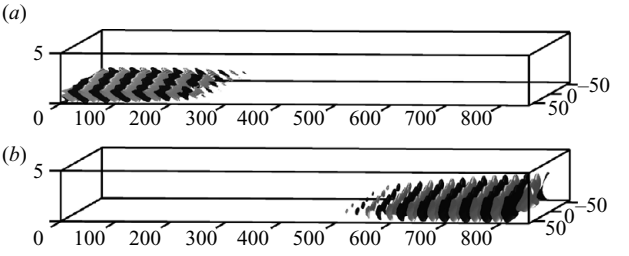


FIGURE 17. Isosurfaces of optimal forcing and response for the streamwise wavenumber $\beta = 0.05$ subject to forcing at the frequency $\omega = 0.055$. Red/blue colour signifies isosurfaces corresponding to positive/negative velocities at 10 % of the maximum. (*a*) Streamwise component of optimal forcing structure. (*b*) Streamwise velocity component of the response.

consist of streamwise elongated streaks induced by cross-stream forcing. At the largest spanwise wavenumbers, we also observe that the decay of the amplification when increasing the forcing frequencies is rather slow. Conversely, the peak corresponding to excitation of the TS-waves is more pronounced.

A visualization of the overall maximum amplification, found for the spanwise wavenumber of $\beta = 0.05$ and for the same frequency $\omega = 0.55$ yielding the optimal two-dimensional forcing, is presented below. The optimal forcing in the streamwise momentum equation and the streamwise velocity component of the optimal response are shown in figure 17. The optimal forcing structures lean against the shear (see figure 17*a*) to optimally trigger the Orr mechanism; the regime long-time response of the flow, shown in figure 17(*b*), reveals the appearance of amplified TS-waves at the downstream end of the computational domain.

The optimal forcing structure at $\beta = 0.6$ and the zero frequency has almost all its energy in the spanwise and wall normal components, that is the flow is forced

https://doi.org/10.1017/S0022112009993703 Published online by Cambridge University Press

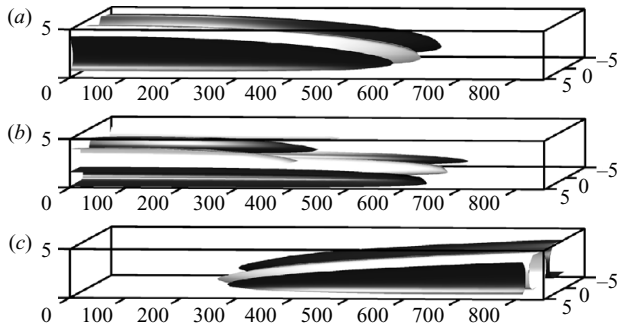


FIGURE 18. Isosurfaces of optimal forcing and response for the streamwise wavenumber $\beta = 0.6$ subject to steady forcing. Red/blue colour indicates isosurfaces corresponding to positive/negative velocities at 10 % of the maximum. (*a*) Wall-normal component of optimal forcing structure. (*b*) Spanwise component of optimal forcing. (*c*) Streamwise velocity component of the flow response. Both the forcing structures and the response are highly elongated in the streamwise direction.

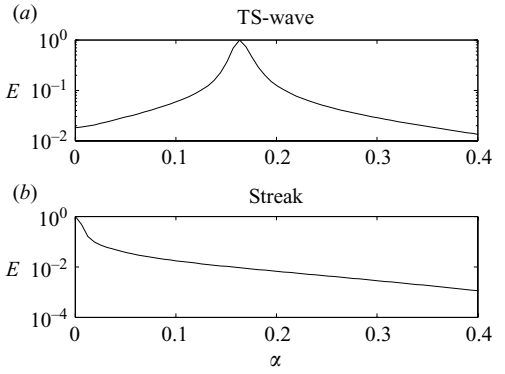


FIGURE 19. Energy spectra along the streamwise direction for the optimal forcing at $\omega = 0.055$, $\beta = 0.05$ (TS-wave) and $\omega = 0$, $\beta = 0.6$ (streak).

optimally in the wall-normal and spanwise directions as shown, among others, by Jovanovic & Bamieh (2005) for channel flows. The wall-normal and spanwise components of the forcing are displayed in figures 18(*a*) and 18(*b*). The r.m.s. values of the streamwise component of the forcing are only 2 % of that of its spanwise and wall-normal counterparts. The lift-up effect transfers momentum into the streamwise component (shown in figure 18*c*), which contains 99.99 % of the energy of the flow response. The streak amplitude increases in the streamwise direction until the fringe region is encountered.

The Fourier transform along the streamwise direction of the two disturbances investigated above is shown in figure 19. As in the case of the optimal initial conditions in figure 8, the energy density is first integrated in the wall-normal and spanwise directions. The results indicate that the TS-wave disturbance has a peak at a relatively high $\alpha \approx 0.17$, whereas the zero-frequency forcing is concentrated at the lowest wavenumbers. The peak at the wavenumber of the most unstable TS-waves is more evident in the case of forcing than in the case of the optimal initial condition (see figure 8).

https://doi.org/10.1017/S0022112009993703 Published online by Cambridge University Press

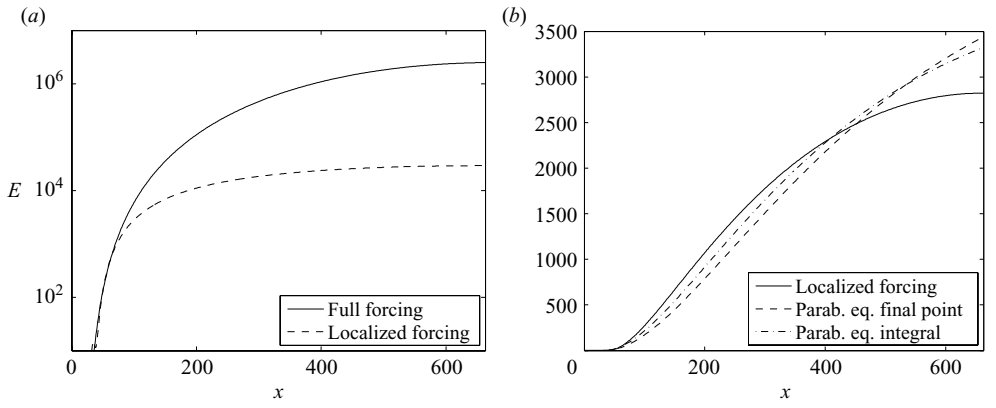


FIGURE 20. Downstream evolution of the kinetic energy of the flow integrated over cross-stream planes. In (*a*), blue and green lines are used to indicate the response to steady forcing active everywhere in the domain (Full forcing) and in a short region near the inflow (localized forcing), respectively. The data are scaled with the magnitude of the forcing computed as integral over the whole domain. In (*b*), the blue line corresponds to the case of localized forcing in (a), whereas green (Parab. eq. final point) indicates the evolution of the optimal initial condition yielding the largest possible kinetic energy at the downstream location $662\delta_0^*$ (Levin & Henningson 2003), and the red line (Parab. eq. integral) indicates the evolution of optimal initial condition yielding the largest integral over the streamwise domain. In order to make a physically relevant comparison, we have scaled the data pertaining to the 'localized forcing' with the value of the response just downstream of the forcing region. The centre of the forcing is at the location $x = 32.3\delta_0^*$ corresponding to the optimal upstream location in Levin & Henningson (2003).

5.2.2. *Localized forcing*

In this section, we present results obtained by restricting the forcing to a small region near the inflow of the computational domain. The formulation presented in § 4 is altered by multiplying the forcing $\boldsymbol{f}$ with a function $\lambda(x)$ which is non-zero only in a short streamwise region. The edges of this region are defined by two smooth step functions rising from zero to one over a distance of about $1\delta_0^*$. The centre of the forcing is chosen to be at $x = 23\delta_0^*$ with width of $4\delta_0^*$, if not otherwise stated.

This problem is physically closer to the case when disturbances are generated upstream, closer to the leading edge, and their evolution is monitored as they are convected downstream. Initially, a comparison with optimal upstream disturbances calculated by means of the parabolized equations is thus presented (see results in Levin & Henningson 2003).

To this aim, we compute the optimal localized steady forcing for spanwise wavenumber $\beta = 0.53$ at $x = 32.3\delta_0^*$. These were found to be the location and spanwise scale of the overall optimal by Levin & Henningson (2003); in their scalings they correspond to $X = 0.37$ and $\beta = 0.53$ for an initial perturbation downstream of the leading edge with Reynolds-number-independent evolution, here assumed to be $Re_x = 10^6$.

In figure 20, the streamwise growth of the energy of the perturbation obtained with four different approaches is shown. In figure 20(*a*), we compare the flow regime response to steady forcing active everywhere in the domain with the response to forcing localized upstream. Furthermore, the localized forcing is compared in figure 20(*b*) with the evolution of the optimal initial conditions yielding the largest possible kinetic energy at the downstream location $662\delta_0^*$ and with the evolution of the optimal

https://doi.org/10.1017/S0022112009993703 Published online by Cambridge University Press

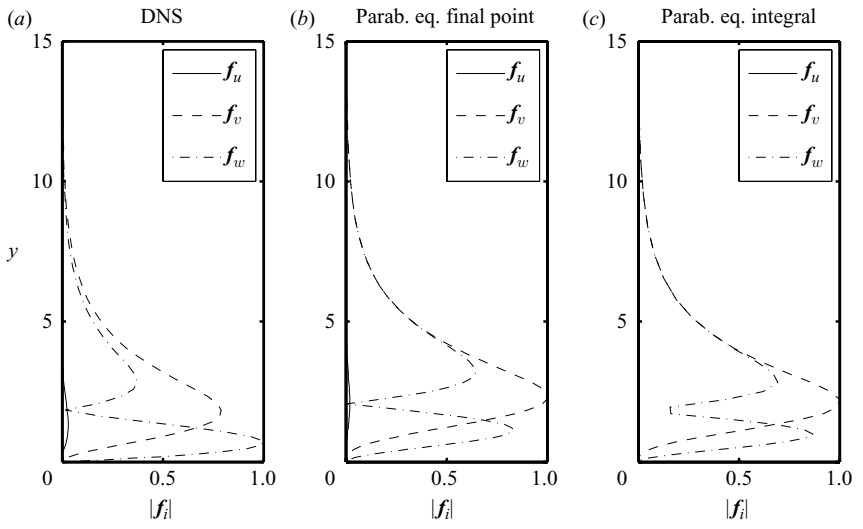


FIGURE 21. Wall-normal profiles of the streamwise, spanwise and wall-normal components of (*a*) the optimal localized forcing (integrated in the streamwise direction), (*b*) the initial condition yielding the largest possible kinetic energy at the downstream location $662\delta_0^*$, (*c*) the initial condition yielding the largest integral of the disturbance energy over the streamwise domain.

upstream velocity profile yielding the largest integral of the perturbation energy over the whole streamwise domain (see also Cathalifaud & Luchini 2000). The two initial condition problems here are computed with the parabolic stability equations (David Tempelmann 2009, private communication); the case having as objective function the integral of the perturbation energy is indeed more relevant for comparison with the present results. It can be seen that the growth is faster when the forcing is active everywhere in our control domain because the component-wise transfer of energy is at work at every streamwise position. The two curves obtained with the parabolic equations (figure 20*a*) are similar: faster growth is observed when the control optimizes over the whole domain, whereas a larger final level is reached when the objective is limited to the last downstream station. The comparison between the response to 'localized forcing' and the 'parabolic equations' cases reveals good agreement. The main differences between the two methods are the different set of equations and the way the disturbance is introduced. In Levin & Henningson (2003) and Cathalifaud & Luchini (2000), the linearized boundary-layer equations are used, whereas we use the Navier–Stokes equations. In addition, an optimal upstream boundary condition is computed by Levin & Henningson (2003), whereas an optimal forcing is sought here.

Figure 21(*a*) displays the structure of the optimal forcing function for the case of localized excitation. The wall-normal profiles shown in the plot are obtained by integrating the forcing in the streamwise direction. Figures 21(*b*) and 21(*c*) depict instead the optimal initial condition obtained with the parabolic boundary-layer equations, i.e. a streamwise vortex pair. The structure of the disturbances is remarkably similar; in the case of the optimal forcing (figure 21*a*), the action is located closer to the wall with a relatively weaker wall-normal component. While comparing the cases in figures 21(*b*) and 21(*c*), one can note that the vortices leading to the largest possible energy downstream are located farther up into the free stream. Conversely, when the perturbations are required to grow over the whole domain, the disturbance needs to

https://doi.org/10.1017/S0022112009993703 Published online by Cambridge University Press

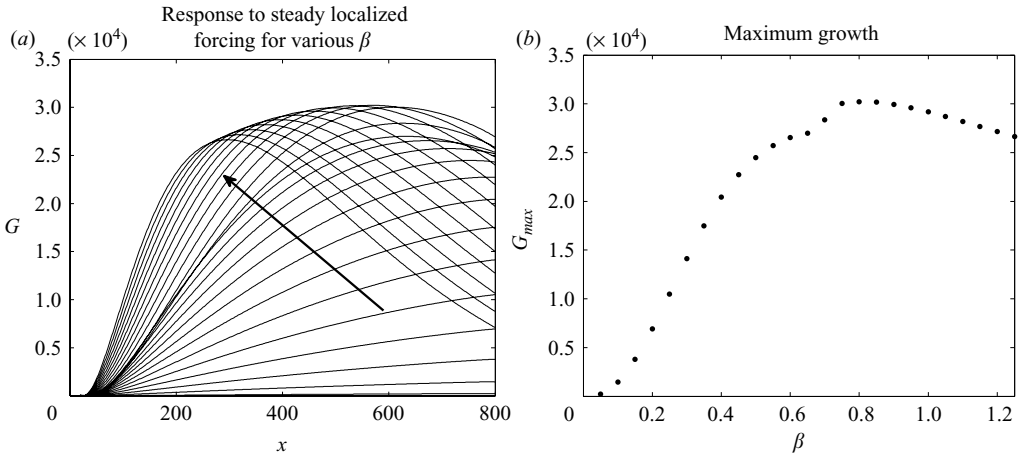


FIGURE 22. (*a*) Streamwise evolution of the response to steady localized forcing for different spanwise wavenumbers β. The arrow indicates increasing β. (*b*) Maximum response versus spanwise wavenumbers.

be located in the shear layer so that its effect can be readily felt (cf. figure 21*a*,*c*). The results in the figure indicate that forcing the momentum equation is less effective in the free stream: optimal forcing thus induces streaks which grow for a shorter downstream distance.

A parameter study is conducted to examine the effect of frequency and spanwise scale of the localized forcing. First, the results obtained when varying the spanwise wavenumber are shown (figure 22). The downstream evolution originating from optimal localized disturbances of zero frequency is displayed for the spanwise wavenumbers investigated. A slower energy growth is observed for the lower wavenumbers owing to the lower forcing to the streaks (proportional to β); the wavenumber giving the largest peak response for the present configuration is $\beta = 0.8$. Forcing of smaller scales induces streaks rapidly, but viscous dissipation causes earlier decay.

As shown by Andersson *et al.* (2001), among others, in the range of validity of the boundary layer equations, there is a coupling between the streamwise and spanwise length scales of the disturbance. It is in fact possible to show that a streak family $u(x, y, z)$, defined by the spanwise wavenumber β_0, is independent of the Reynolds number. This results in a scaling property that couples the streamwise and spanwise scales, implying that the same solution is valid for every combination of the streamwise location $x + x_0$ (distance from the leading edge) and of β such that their product stays constant. In other words, this amounts to moving along the plate and varying the spanwise wavenumber so that the local spanwise wavenumber $\beta_0\delta^*/\delta_0^*$ remains constant (see also Brandt *et al.* 2003). To further examine this scaling property, the streamwise coordinate in figure 22(*a*) is multiplied by the spanwise wavenumber of the disturbance and the result is shown in figure 23. Despite the fact that the streamwise extent of each curve is different, the curves indicating the evolution of the streaky disturbance collapse notably, thus confirming the similarity of the boundary-layer streaks.

Finally, we investigate the case of zero spanwise number (pure two-dimensional disturbances) and vary the temporal frequency. The results are shown in figure 24. The growth observed here is due to the combined Orr and TS-wave mechanism, and

https://doi.org/10.1017/S0022112009993703 Published online by Cambridge University Press

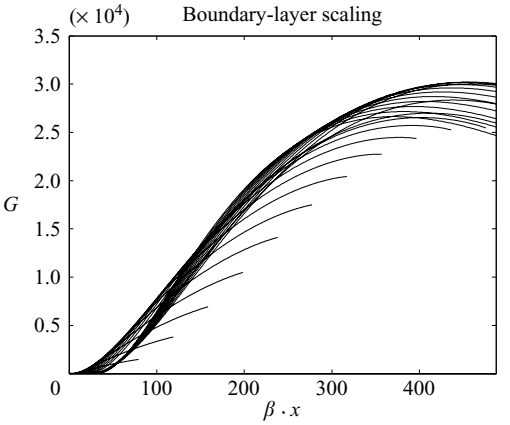


FIGURE 23. Streamwise evolution of the response to localized forcing for different spanwise wavenumbers β where the streamwise position x is scaled with β. The distance from the leading edge is considered to rescale the data.

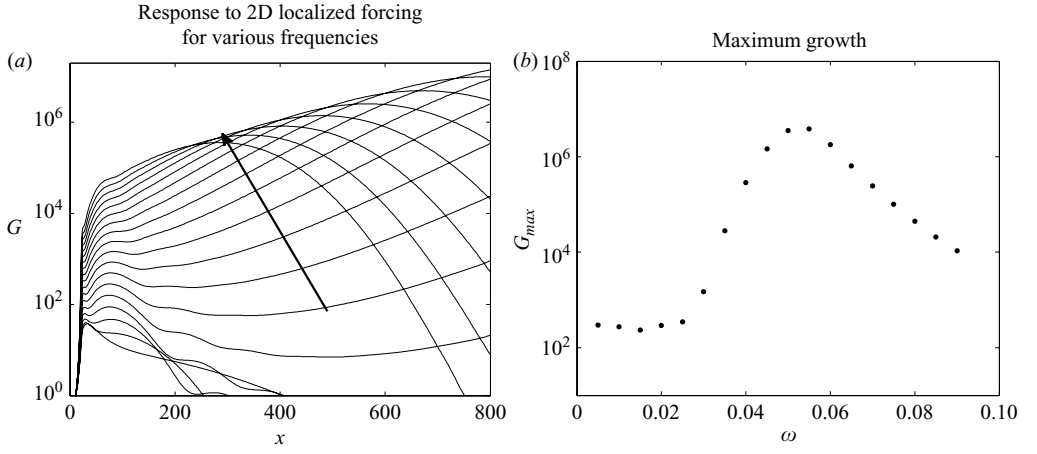


FIGURE 24. (a) Streamwise evolution of the response to localized forcing for different temporal frequencies ω. The arrow indicates increasing ω. (b) Maximum growth with respect to ω. The spanwise wavenumber is $\beta = 0$.

thus the value of the optimal frequency is close to that obtained when forcing over the whole domain, $\omega = 0.055$. The structure of the optimal forcing for the frequency with largest amplification is displayed in figure 25. The excitation is localized closer to the wall, well inside the boundary layer, when compared to the forcing forming streamwise streaks; see figure 21. Forcing the streamwise momentum equation is significantly more efficient at triggering the Orr mechanism and the subsequent wave packet of two-dimensional TS-waves.

6. Conclusions

We have used a Lagrange multiplier technique in conjunction with direct and adjoint linearized Navier–Stokes equations in order to quantify the growth potential in the spatially developing flat-plate boundary-layer flow at moderately high Reynolds.

https://doi.org/10.1017/S0022112009993703 Published online by Cambridge University Press

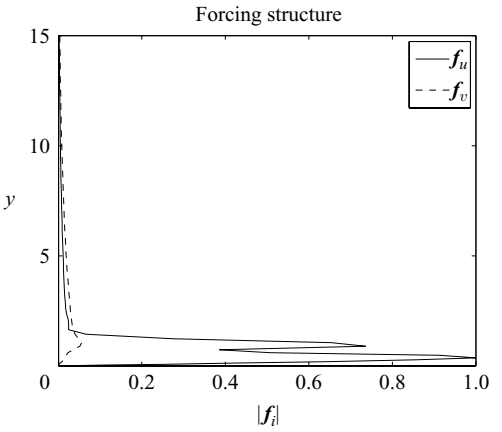


FIGURE 25. Localized forcing with frequency. We plot the streamwise and wall-normal components of the forcing function. The quantities are integrated in the streamwise direction. Note that this is a two-dimensional structure, thus the spanwise component is zero.

Spanwise periodic and fully three-dimensional disturbances are investigated. We consider both the initial conditions leading to the largest possible energy amplification at time T and the optimal spatial structure of time-periodic forcing. To the best of our knowledge, the pseudo-spectrum of the governing operator along real frequencies is computed here for the first time with matrix-free methods. The optimization framework adopted does not restrict us to assume slow variation of the base flow in the streamwise direction, common to both the first-order approximation of the OSS formulation and the more advanced parabolic stability equations (PSE) approximation. Specifically, we do not, as in the PSE framework, need different equations to describe the lift-up instability and the wave packet propagation.

For the optimal initial condition we find that the largest potential for growth is found at small spanwise wavenumbers and consists of upstream tilted structures, enabling the subsequent disturbances to exploit the Orr mechanism and the local convective instability of the oblique wave packet of TS-waves. The length and position of the initial disturbance is related to the final time of the optimization: short time evolution requires the wave packet to be initiated farther downstream in the region of largest local instability and vice versa for longer optimization times. The lift-up instability mechanism inherent to spanwise wavelengths of the order of the boundary-layer thickness is faster than the Orr/oblique instability; for the present configuration, the streaks reach their maximum energy earlier; conversely, the TS-wave instability needs more time to extract the same amount of energy, at the same time travelling a shorter distance. The evolution of the kinetic energy of these two perturbations in time and space is displayed in figure 26.

The results further indicate that streamwise vortices of finite length become optimal once a spatially evolving boundary layer with inflow/outflow conditions is considered. As concerns the optimal response to periodic forcing, the difference in the two instabilities is less pronounced. In this case, the Orr/oblique wave instability only manages to gain a factor of two in energy more than the streak mechanism. The largest amplification of the local convective instability over the non-modal streak generation can be explained by the long computational box examined and the relatively high inflow Reynolds number. Starting closer to the leading edge, one can expect streaks to become more relevant.

https://doi.org/10.1017/S0022112009993703 Published online by Cambridge University Press

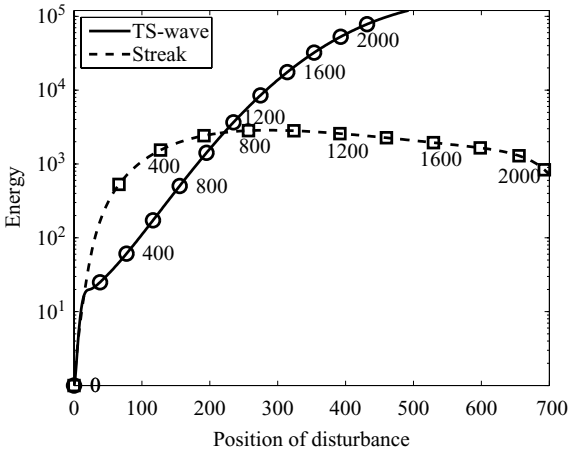


FIGURE 26. Evolution of the kinetic energy of the two optimal initial perturbations for $t = 720$ (streaks) and $t = 1820$ (TS-waves) versus the current spatial position. The position of the disturbance is computed by tracking its 'centre of mass' using the kinetic energy as density. The numbers beside the markers correspond to time instances.

Three-dimensional localized optimal initial conditions are also computed and the corresponding wave packets examined. For short optimization times, the optimal disturbances consist of streaky structures propagating and elongating downstream without any significant spreading in the lateral direction. For long optimization times, conversely, the optimal disturbances are characterized by wave packets of TS-waves. These travel at lower streamwise speed and with faster spreading in the spanwise direction. The TS-wave packet can achieve the largest possible energy amplification. Intermediate optimization times are also considered where both the TS- and streak mechanisms are relevant. The wave packet has therefore features from both scenarios previously considered: It consists of elongated streaks in the streamwise velocity component, followed by short-wavelength instability waves, mainly evident in the cross-stream velocities.

Finally, we examine the effect of upstream disturbances on the boundary-layer flow. Thus, we introduce a localized forcing near the inflow of the computational box and compute the forcing structure that provides the largest response over our control domain. First, we compare with results based on the solution of the parabolized Navier–Stokes equations: good agreement is obtained despite the differences between the two methods. Second, we investigate zero-frequency upstream forcing and show a maximum for perturbations with spanwise wavenumber larger than that obtained when the forcing location is not constrained. Third, an analysis of time-periodic two-dimensional forcing is considered: the findings agree with those obtained with distributed forcing because the flow response corresponds in both cases to exponentially growing TS-waves at the forcing frequency.

Three different destabilizing mechanisms are considered in this study, all at work in the boundary layer flow. Although these could be explained using the OSS equations, they are analysed without any simplifying assumptions. This work is of a more general character. By choosing an objective function and using the full linearized Navier–Stokes equations as constraints, we are not limiting ourselves to simple geometries. Whenever a DNS code is available to accurately describe a flow, all that is needed in order to investigate the stability characteristics is a linearized version of the

https://doi.org/10.1017/S0022112009993703 Published online by Cambridge University Press

code and the implementation of the corresponding adjoint equations along with a wrapper ensuring the correct optimization scheme. The method used here is therefore applicable to any geometrical configuration.

The authors wish to thank David Tempelmann for providing data from the parabolic stability equations and many fruitful discussions and Carlo Cossu for inspiring comments on the manuscript. Computer time provided by SNIC (Swedish National Infrastructure for Computing) is gratefully acknowledged. This work is supported by the Swedish Research Council (VR).

REFERENCES

Åkervik, E., Ehrenstein, U., Gallaire, F. & Henningson, D. S. 2008 Global two-dimensional stability measures of the flat plate boundary-layer flow. *Eur. J. Mech.* B. *Fluids* **27**, 501–513.

Åkervik, E., Hœpffner, J., Ehrenstein, U. & Henningson, D. S. 2007 Optimal growth, model reduction and control in a separated boundary-layer flow using global eigenmodes. *J. Fluid Mech.* **579**, 305–314.

Alizard, F., Cherubini, S. & Robinet, J.-C. 2009 Sensitivity and optimal forcing response in separated boundary layer flows. *Phys. Fluids* **21**, 064108.

Andersson, P., Berggren, M. & Henningson, D. S. 1999 Optimal disturbances and bypass transition in boundary layers. *Phys. Fluids* **11**, 134–150.

Andersson, P., Brandt, L., Bottaro, A. & Henningson, D. S. 2001 On the breakdown of boundary layers streaks. *J. Fluid Mech.* **428**, 29–60.

Bagheri, S., Åkervik, E., Brandt, L. & Henningson, D. S. 2009*a* Matrix-free methods for the stability and control of boundary layers. *AIAA J.* **47**, 1057–1068.

Bagheri, S., Brandt, L. & Henningson, D. S. 2009*b* Input–output analysis, model reduction and control of the flat-plate boundary layer. *J. Fluid Mech.* **620**, 263–298.

Barkley, D., Blackburn, H. M. & Sherwin, S. J. 2008 Direct optimal growth analysis for timesteppers. *Intl J. Numer. Meth. Fluids* **57**, 1435–1458.

Blackburn, H. M., Barkley, D. & Sherwin, S. J. 2008 Convective instability and transient growth in flow over a backward-facing step. *J. Fluid Mech.* **608**, 271–304.

Brandt, L., Cossu, C., Chomaz, J.-M., Huerre, P. & Henningson, D. S. 2003 On the convectively unstable nature of optimal streaks in boundary layers. *J. Fluid Mech.* **485**, 221–242.

Butler, K. M. & Farrell, B. F. 1992 Three-dimensional optimal perturbations in viscous shear flow. *Phys. Fluids* A **4**, 1637–1650.

Cathalifaud, P. & Luchini, P. 2000 Algebraic growth in boundary layers: optimal control by blowing and suction at the wall. *Eur. J. Mech.* B. *Fluids* **19**, 469–490.

Chevalier, M., Schlatter, P., Lundbladh, A. & Henningson, D. S. 2007 A pseudo spectral solver for incompressible boundary layer flows. *Tech. Rep.* Trita-Mek **7**.

Chomaz, J. M. 2005 Global instabilities in spatially developing flows: non-normality and nonlinearity. *Annu. Rev. Fluid Mech.* **37**, 357–392.

Corbett, P. & Bottaro, A. 2000 Optimal perturbations for boundary layers subject to streamwise pressure gradient. *Phys. Fluids* **12** (1), 120–130.

Cossu, C. & Chomaz, J. M. 1997 Global measures of local convective instability. *Phys. Rev. Lett.* **77**, 4387–90.

Ehrenstein, U. & Gallaire, F. 2005 On two-dimensional temporal modes in spatially evolving open flows: the flat-plate boundary layer. *J. Fluid Mech.* **536**, 209–218.

Ehrenstein, U. & Gallaire, F. 2008 Two-dimensional global low-frequency oscillations in a separating boundary-layer flow. *J. Fluid Mech.* **614**, 315–327.

Ellingsen, T. & Palm, E. 1975 Stability of linear flow. *Phys. Fluids* **18**, 487–488.

Gallaire, F., Marquillie, M. & Ehrenstein, U. 2007 Three-dimensional transverse instabilities in detached boundary layers. *J. Fluid Mech.* **571**, 221–233.

Gaster, M. 1975 A theoretical model of a wave packet in a boundary layer over a flat plate. *Proc. R. Soc. London, Ser.* A **347**, 271–289.

https://doi.org/10.1017/S0022112009993703 Published online by Cambridge University Press

Gaster, M. & Grant, I. 1975 An experimental investigation of the formation and development of a wave packet in a laminar boundary layer. *Proc. R. Soc. London, Ser.* A **347**, 253–269.

Jovanovic, M. R. & Bamieh, B. 2005 Componentwise energy amplification in channel flows. *J. Fluid Mech.* **534**, 145–183.

Koch, W. 2002 On the spatio-temporal stability of primary and secondary crossflow vortices in a three-dimensional boundary layer. *J. Fluid Mech.* **456**, 85–111.

Kreiss, G., Lundbladh, A. & Henningson, D. S. 1994 Bounds for treshold amplitudes in subcritical shear flows. *J. Fluid Mech.* **270**, 175–198.

Landahl, M. T. 1980 A note on an algebraic instability of inviscid parallel shear flows. *J. Fluid Mech.* **98**, 1–34.

Lehoucq, R. B., Sorensen, D. & Yang, C. 1997 Arpack users' guide: solution of large scale eigenvalue problems with implicitly restarted Arnoldi methods. *Tech. Rep.* from http://www.caam.rice.edu/software/ARPACK/, Computational and Applied Mathematics, Rice University.

Levin, O. & Henningson, D. S. 2003 Exponential vs algebraic growth and transition prediction in boundary layer flow. *Flow Turbul. Combust.* **70**, 183–210.

Luchini, P. 2000 Reynolds-number-independent instability of the boundary layer over a flat surface: optimal perturbations. *J. Fluid Mech.* **404**, 289–309.

Lundell, F. & Alfredsson, P. H. 2004 Streamwise scaling of streaks in laminar boundary layers subjected to free-stream turbulence. *Phys. Fluids* **16** (5), 1814–1817.

Mamun, C. K. & Tuckerman, L. S. 1995 Asymmetry and Hopf bifurcation in spherical Couette flow. *Phys. Fluids* **7** (1), 80–91.

Marcus, P. S. & Tuckerman, L. S. 1987*a* Simulation of flow between concentric rotating spheres. Part 1. Steady states. *J. Fluid Mech.* **185**, 1–30.

Marcus, P. S. & Tuckerman, L. S. 1987*b* Simulation of flow between concentric rotating spheres. Part 2. Transitions. *J. Fluid Mech.* **185**, 31–65.

Marquet, O., Lombardi, M., Chomaz, J. M., Sipp, D. & Jacquin, L. 2009 Direct and adjoint global modes of a recirculation bubble: lift-up and convective non-normalities. *J. Fluid Mech.* **622**, 1–21.

Marquet, O., Sipp, D., Chomaz, J. M. & Jacquin, L. 2008 Amplifier and resonator dynamics of a low-Reynolds-number recirculation bubble in a global framework. *J. Fluid Mech.* **605**, 429–443.

Nayar, M. & Ortega, U. 1993 Computation of selected eigenvalues of generalized eigenvalue problems. *J. Comput. Phys.* **108**, 8–14.

Nordström, J., Nordin, N. & Henningson, D. S. 1999 The fringe region technique and the Fourier method used in the direct numerical simulation of spatially evolving viscous flows. *SIAM J. Sci. Comp.* **20**, 1365–1393.

Orr, W. M. F. 1907 The stability or instability of the steady motions of a perfect liquid and of a viscous liquid. Part I: A perfect liquid. Part II: A viscous liquid. *Proc. R. Irish Acad.* A **27**, 9–138.

Reddy, S. C. & Henningson, D. S. 1993 Energy growth in viscous channel flows. *J. Fluid Mech.* **252**, 209–238.

Schmid, P. J. & Henningson, D. S. 2001 *Stability and Transition in Shear Flows*. Springer.

Trefethen, L. N., Trefethen, A. E., Reddy, S. C. & Driscoll, T. A. 1993 Hydrodynamic stability without eigenvalues. *Science* **261**, 578–584.

Trefethen, N. & Embree, M. 2005 *Spectra and Pseudospectra: The Behaviour of Nonnormal Matrices and Operators*. Princeton University Press.

Tuckerman, L. S. & Barkley, D. 2000 Bifurcation analysis for timesteppers. In *Numerical Methods for Bifurcation Problems and Large-Scale Dynamical Systems*, pp. 453–566. Springer.

https://doi.org/10.1017/S0022112009993703 Published online by Cambridge University Press